
Doctoral Dissertations

Student Theses and Dissertations

Fall 2017

Modal based BGA modeling in high-speed package

Shuai Jin

Follow this and additional works at: https://scholarsmine.mst.edu/doctoral_dissertations



Part of the [Electromagnetics and Photonics Commons](#)

Department: **Electrical and Computer Engineering**

Recommended Citation

Jin, Shuai, "Modal based BGA modeling in high-speed package" (2017). *Doctoral Dissertations*. 2624.
https://scholarsmine.mst.edu/doctoral_dissertations/2624

This thesis is brought to you by Scholars' Mine, a service of the Missouri S&T Library and Learning Resources. This work is protected by U. S. Copyright Law. Unauthorized use including reproduction for redistribution requires the permission of the copyright holder. For more information, please contact scholarsmine@mst.edu.

MODAL BASED BGA MODELING IN HIGH-SPEED PACKAGE

by

SHUAI JIN

A DISSERTATION

Presented to the Faculty of the Graduate School of the
MISSOURI UNIVERSITY OF SCIENCE AND TECHNOLOGY

In Partial Fulfillment of the Requirements for the Degree

DOCTOR OF PHILOSOPHY

in

ELECTRICAL ENGINEERING

2017

Approved by

Dr. Jun Fan, Advisor
Dr. James L. Drewniak
Dr. Daryl Beetner
Dr. David Pommerenke
Dr. Matthew J. O'Keefe

© 2017

Shuai Jin

All Rights Reserved

ABSTRACT

In the Section 1, the improved “Root-Omega” method for extracting dielectric properties from fabricated multilayer printed circuit boards is proposed. Based on the electrical properties of fabricated transmission lines, the improved “Root-Omega” method applied to cases with smooth and rough conductors is validated using simulations. Error sensitivity analysis is performed to demonstrate the potential errors in the original “Root-Omega” procedure and the error sensitivity is significantly reduced by the proposed improvements.

In the Section 2, a fast modal-based approach is developed to accurately and efficiently capture the proximity effect. Image theory is also applied in the proposed approach to reduce the computational domain from 3D structure to 2D. The matrix reduction approach is applied to obtain the physical loop inductance. The lumped capacitance is obtained. A π topology equivalent circuit model for the BGA structure is built. Good agreement between the equivalent circuit model and full wave simulation can be achieved up to 40GHz.

In the Section 3, the proximity effect for BGAs between parallel plates is carefully considered. A modal-based cavity method is proposed to extract the partial inductance of two parallel plates. The modal basis function is used to count for the non-uniformly distributed current density. The physical loop inductance is further obtained from the matrix reduction approach. The extracted physical loop inductance is validated with a commercial finite element method-based tool. The boundary effect is demonstrated in the inductance extraction. The proposed method is used to optimize for the power distributed network design.

ACKNOWLEDGMENTS

In the Section 1, the improved “Root-Omega” method for extracting dielectric I would like to express my sincere gratitude to Dr. Jun Fan, my advisor, for accepting me into his group and for his teaching, instruction, warm encouragement on my research work, financial support to my study and direction for this dissertation during my pursuit of the PhD’s degree.

I would like to thank Dr. James Drewniak for the encouragement on my study, helpful suggestions on my dissertation and enlightening the way to the future.

I would like to thank Dr. Daryl Beetner for teaching in my courses, discussions related to my research and helpful suggestions during my PhD degree.

I would like to thank Dr. David Pommerenke for his enlightening to my research motion and teaching me great skills in doing research.

I would like to thank Dr. Matthew J. O’Keefe for his insightful comments during the PhD’s degree.

I would also like to express my thanks to all the other faculty members and students in UMR/MST EMC lab for their team work and help in my research and coursework. It has been my great pleasure to work with you.

This dissertation is based upon work supported partially by the National Science Foundation under Grant No. IIP-1440110.

Finally, I would like to thank my family for their love and my wife Han for her unconditional support during my five years of graduate study.

TABLE OF CONTENTS

	Page
ABSTRACT.....	iii
ACKNOWLEDGMENTS	iv
LIST OF ILLUSTRATIONS.....	vii
LIST OF TABLES.....	ix
SECTION	
1. MATERIAL PROPERTY EXTRACTION FOR MULTILAYER PCBS.....	1
1.1. ORIGINAL METHOD LIMITATIONS	4
1.1.1. The Root Omega Method.....	5
1.1.1.1 Smooth conductor.....	5
1.1.1.2 Rough conductor.....	5
1.1.2. Limitations.....	7
1.1.2.1 Dielectric property extraction for smooth conductor.....	7
1.1.2.2 Dielectric property extraction for rough conductor	12
1.1.3. Error Sensitivity Analysis of the Root-Omega Method	12
1.2. THE IMPROVED METHOD AND ERROR ANALYSIS	15
1.2.1. The Improved Root-Omega Method	16
1.2.1.1 The improved root-omega method for smooth conductor	16
1.2.1.2 The improved root-omega method for rough conductor.....	21
1.2.2. Validation of the Improved Root-Omega Method	22
1.2.2.1 Dielectric property extraction	22
1.2.2.2 Dielectric property extraction for rough conductor	26
1.2.3. Error Sensitivity Analysis of the Improved Root-Omega Method.....	29
2. MODAL BASED BGA MODELING	31
2.1. METHODOLOGY OF EQUIVALENT INDUCTANCE CALCULATION ..	32
2.1.1. Basis Functions.....	33
2.1.2. Modal Based Partial Inductance	34
2.1.3. Evaluation of Partial Inductance Element and System Matrix.....	38
2.1.4. Equivalent Loop Inductance for Signal and Ground Balls.....	39

2.1.5. Equivalent Loop Inductance for Power and Ground Balls.....	42
2.2. EQUIVALENT CAPACITANCE CALCULATION.....	43
2.3. EQUIVALENT CIRCUIT FOR SIGNAL AND GROUND BALLS	45
2.4. GUIDELINE FOR POWER GROUND BALL PATTERN.....	48
3. MODAL BASED INDUCTANCE EXTRACTION.....	51
3.1. METHODOLOGY OF EQUIVALENT INDUCTANCE CALCULATION ..	52
3.1.1. Basis Functions.....	53
3.1.2. Modal-based Partial Inductance from Cavity Method	53
3.1.3. System Matrix Calculation.....	58
3.1.4. Physical Loop Inductance Extraction.	63
3.2. EQUIVALENT INDUCTANCE VALIDATION	66
BIBLIOGRAPHY.....	71
VITA	80

LIST OF ILLUSTRATIONS

	Page
Figure 1.1. Illustration of the cross section of a rough stripline	8
Figure 1.2. Flowchart of the “root-omega” method.....	8
Figure 1.3. Cross section of the narrow trace	9
Figure 1.4. Cross section of the wide trace.....	9
Figure 1.5. Validation of S-parameters.....	9
Figure 1.6. Dk and Df extraction for a large Df material	10
Figure 1.7. Dk and Df extraction for a small Df material.....	11
Figure 1.8. Different extracted Df values at different frequencies	12
Figure 1.9. Cross section of the rough narrow trace	13
Figure 1.10. Cross section of the rough narrow trace.....	13
Figure 1.11. Dk and Df extraction for a large Df material from two rough traces	13
Figure 1.12. Dk and Df extraction for a small Df material from two rough traces	14
Figure 1.13. The procedure of Dk and Df extraction for smooth conductor	20
Figure 1.14. The procedure of Dk and Df extraction for rough conductor.....	23
Figure 1.15. Flowchart of the improved “root-omega” method	24
Figure 1.16. Illustration of the cross section of two smooth striplines	24
Figure 1.17. Validation of extracted Dk and Df in wide trace.....	25
Figure 1.18. Validation of extracted Dk and Df in narrow trace	25
Figure 1.19. Extracted Df with different cut frequency.....	26
Figure 1.20. Illustration of the cross section of two rough stripline	27
Figure 1.21. Validation of extracted Dk and Df in rough trace	27
Figure 1.22. Cross section geometry of narrow and wide trace.....	28
Figure 1.23. Validation of extracted Dk and Df in rough trace	29
Figure 2.1. The signal and ground BGA balls are in between two parallel plates.....	32
Figure 2.2. The BGA balls between two parallel plates	33
Figure 2.3. Two basis functions are in the same local coordinate	38
Figure 2.4. Two basis functions are in the different local coordinate.....	39
Figure 2.5. The illustration of voltage and current for BGA balls.....	39

Figure 2.6. Illustration figure for power and ground net	42
Figure 2.7. Segmentation of BGA balls and a parallel plate pair	43
Figure 2.8. The equivalent circuit model for BGA balls	45
Figure 2.9. BGA ball structures in full-wave simulator.....	46
Figure 2.10. Comparison of differential mode S-parameters	47
Figure 2.11. Comparison of common mode S-parameters	48
Figure 2.12. Different power ground ball patterns	49
Figure 3.1. Parallel plate structure with BGA balls	52
Figure 3.2. Rectangular cavity structure with circular ports.....	56
Figure 3.3. The illustration of voltage and current for BGA balls.....	63
Figure 3.4. Parallel plate with one power ball and one ground ball	66
Figure 3.5. Equivalent loop inductance converges with number of modes increased.....	67
Figure 3.6. Equivalent inductance (pH) for column patterns.....	68
Figure 3.7. Equivalent inductance (pH) for row patterns	68
Figure 3.8. Column BGA ball patterns	69
Figure 3.9. Alternate BGA ball patterns	69

LIST OF TABLES

	Page
Table 1.1. Huray roughness model settings	28
Table 2.1. Inductance validation between analytical method and full-wave simulation..	46
Table 2.2. Equivalent inductance from column pattern	49
Table 2.3. Equivalent inductance from alternate pattern	49
Table 3.1. Modal inductance element	64
Table 3.2. Inductance validation between proposed method and standard.....	67
Table 3.3 Equivalent inductance for different patterns.....	70

1. MATERIAL PROPERTY EXTRACTION FOR MULTILAYER PCBS

Dielectric material plays an important role in signal integrity (SI) and power integrity (PI) [1]-[5]. For example, when designing channels in high-speed products, the geometry and dielectric material properties determine the electrical performance, such as the network parameters, eye diagram, radiation patterns, and so on. Design optimizations are often carried out and material choice is usually made as a trade-off between electrical performance and cost [6]-[8]. If the material properties are not correct or not accurate enough, the design could either fail to meet the performance specifications resulting in a costly re-spin, or become over-designed by using a more costly, higher performance board material, or the deembedding fixture may fail to work[9]-[11].

Material vendors usually provide the material properties measured for the raw material by the open-ended coaxial probing method [12]-[15], waveguide method [16]-[19], free space method [20] and resonant cavity method [21][22]. The open-ended coaxial probe method is a non-destructive, broadband, temperature controlled testing method. The coaxial probe is immersed into a liquid or intimately pressed against the flat surface of the testing specimen. The reflection coefficient is measured by a vector network analyzer (VNA) and is used to calculate material permittivity [12][13]. However, this method is not suitable for low dielectric property, anisotropic or nonhomogeneous materials and the sample must be thick enough to be treated as infinite seen from the probe. When the surface of the solid sample is not flat or doesn't match with the probe, air gap between sample and probe results in significant errors in the extracted material permittivity [15].

The waveguide method is carried out by placing a piece of sample inside a coaxial line, or waveguide, and measuring the reflection coefficient and transmission coefficient by VNA. The dielectric properties are computed by the scattering parameters [15]-[19]. Compared to the open-ended coaxial probe method, it can be used to measure anisotropic materials in a wide frequency range. However, the samples require machining to be fully occupied in the fixture cross section in the waveguide structure and there should be no air

gap between the fixture wall and samples. The surface also needs to be flat and perpendicular to the ports at two ends of the waveguide. Low accuracy could occur when the length of the sample is the multiple of one-half wavelength in the material.

The free space method can be performed in high temperature or hostile environments with two antennas facing each other and a large, flat sample in between. Two port scattering parameters are measured and computed for dielectric properties [20]. The measurement data and the corresponding dielectric substrate properties can be highly dependent on the applied field direction [13]. In practical products the field distribution may not be the same as in measurement, so the discrepancy may show up.

The resonant cavity method is mostly based on the perturbation method (PM). It compares the resonant frequency and quality factor of an empty resonator and a partially loaded resonator to extract dielectric substrate properties at the operating frequency [21][22]. The cross sectional geometry of the sample must be accurately known. When the conductor loss in the wall of resonator is comparable to the dielectric loss of the sample, the hybrid high-order mode or special calibration is required in the resonant cavity method [22][23]. It is limited as a narrow band method for characterizing dielectric properties. To cover a certain frequency band for the material, multiple test fixtures and resonators are needed.

Another resonant cavity method based on a stripline cavity is specified in IPC-TM-650 [24]. In this IPC-TM-650 test method, the resonant frequency, half power frequency and Q factor are measured to calculate the dielectric constant and dissipation factor. It is intended for the X-band substrate property extraction. The anisotropy of the test specimen and air gap between the specimen and the test pattern may result in errors. To measure material of different permittivity, different test pattern shall be designed which is not only time consuming but also costly. Even though the test pattern is fabricated, the specimen itself is still raw material before printed circuit board (PCB) fabrication.

All these methods deal with raw dielectric materials before a multilayer PCB is fabricated. The extracted material properties provide references but usually are not accurate enough for high-speed design.

When multiple dielectric layers are fabricated together to form a multilayer PCB, the effective dielectric properties after fabrication may become different due to fabrication processes [25]-[29]. Extracting material properties after fabrication is more meaningful for board designers. PCB resonant cavities constructed of parallel planes and stitching vias in a fabricated multilayer PCB can be used to extract substrate properties. However, the dielectric constant (Dk) and dissipation factor (Df) extracted from the cavity methods are inherently narrow band.

Transmission line covers a wide frequency band. It can be used to characterize wide band dielectric properties [25]-[28]. A transmission-line based method was proposed and adopted in the high-speed industry [30]-[37]. It is based on the frequency behaviors of the attenuation factor α and the propagation constant β of a stripline. The conductor attenuation factor α_C and the dielectric attenuation factor α_D have different frequency dependencies. Thus, they can be separated by curve fitting. Same for β_C and β_D . The extracted dielectric attenuation factor α_D and dielectric propagation factor β_D are then used to calculate the dielectric constant (Dk) and the loss tangent (Df). The so-called “Root-Omega” method was further extended to include the conductor surface roughness effects. Two transmission lines of narrow and wide trace widths are used to distinguish the effects of the conductor surface roughness from the dielectric effects [26]. Recently it is found that the “Root-Omega” method could generate different Dk and Df values with different stop-frequency values in the measured data for the same device under test. In other words, the extracted Dk and Df values could be inaccurate and inconsistent depending on the frequency band used in the measurement. Also, the “Root-Omega” method doesn’t work well with low-loss materials. Large errors can be induced in the extracted Df values for materials with a loss tangent smaller than 0.01.

Thus, in this paper, an improved “Root-Omega” method is proposed to address these issues. First of all, a more accurate mathematical model is introduced based on the transmission-line theory, which significantly reduces the effect of the stop frequency on the Dk and Df extraction. Then, an iteration procedure is developed to further improve the accuracy of the extracted Dk and Df values, especially for low loss materials. The performance of the improved method is validated with simulation examples. A simple error analysis is conducted to explain the improvement in terms of extraction accuracy.

1.1. ORIGINAL METHOD LIMITATIONS

This method is based on the S-parameters of a stripline, which should reflect the electrical behaviour of the transmission-line only. The transmission line S-parameters are assumed ideal without measurement errors. Then, the extracted Dk and Df values are the equivalent parameters of the dielectric layers that form the stripline.

The S-parameters are then converted to the ABCD parameters, and the complex propagation constant is calculated as

$$\gamma = \frac{\cosh^{-1}(\sqrt{A \cdot D})}{\text{line length}}; \text{ and } \gamma = \alpha_T + j\beta_T, \quad (1)$$

$$\text{where } \begin{bmatrix} A & B \\ C & D \end{bmatrix} = \begin{bmatrix} \cosh(\gamma l) & Z_0 \sinh(\gamma l) \\ \frac{1}{Z_0 \sinh(\gamma l)} & \cosh(\gamma l) \end{bmatrix}$$

α_T and β_T are the total attenuation factor and the total propagation constant of the stripline

After the total attenuation factor and propagation constant are obtained, they are used to extract the dielectric contributions. The equivalent Dk and Df values of the dielectric media where the traces are located are calculated from the dielectric attenuation factor α_D and the dielectric propagation constant β_D as [26].

$$Dk = \varepsilon'_r = x \sqrt{\frac{x}{x+y}}, \quad (2)$$

$$Df = \frac{\varepsilon''_r}{\varepsilon'_r} = \sqrt{\frac{y}{x}},$$

where $x = \left(\frac{\beta_D v_{free}}{\omega}\right)^2$, and $y = \left(\frac{2v_{free} \alpha_D}{\omega}\right)^2$. v_{free} and ω are the free-space velocity and the

angular frequency, respectively. The extraction procedure for the dielectric contributions is briefly repeated below for further discussions.

1.1.1. The Root Omega Method. The original Root-Omega” method is introduced below.

1.1.1.1 Smooth conductor. In the “Root-Omega” method, when the conductor surface was assumed to be smooth, the total attenuation factor and propagation constant could be separated into two portions. The total attenuation constant α_T can be fitted as

$$\alpha_C = a\sqrt{\omega} \quad (4)$$

$$\alpha_D = b\omega + d\omega^2 \quad (5)$$

Under this assumption, a curve fitting function was used to separate the dielectric loss from the conductor loss. β_D was similarly obtained as

$$\begin{cases} \beta_C = a'\sqrt{\omega} \\ \beta_D = b'\omega + d'\omega^2 \end{cases} \quad (6)$$

When α_D and β_D were obtained, Dk and Df could be calculated by (2).

1.1.1.2 Rough conductor. In the “Root-Omega” method, when the conductor surface is rough, the total attenuator factor and propagation constant have the smooth conductor, rough conductor, and dielectric contributions. The total attenuation factor can be written as

$$\begin{aligned} \alpha_T &= \alpha_{C0} + \alpha_D + \alpha_{Cr} \\ &= (a_1\sqrt{\omega}) + (b_1\omega + d_1\omega^2) + (a_2\sqrt{\omega} + b_2\omega + d_2\omega^2) \\ &= (a_1 + a_2)\sqrt{\omega} + (b_1 + b_2)\omega + (d_1 + d_2)\omega^2 \end{aligned} \quad (7)$$

where a_1 is the coefficient for the smooth-conductor contribution α_C ; b_1 , d_1 are coefficients for the dielectric contribution α_D and a_2 , b_2 , d_2 are coefficients for rough-conductor contribution α_{Cr} .

Since the rough conductor contribution had a similar frequency dependency, it needed two striplines with different geometries (for example, widths) to further

distinguish them. These two traces, narrow and wide for example, have the same dielectric contributions, which means b_1^N and d_1^N are equal to b_1^W and d_1^W , respectively, in the following expressions where the total attenuation factors for the narrow and wide traces are curve fitted into the three terms individually.

$$\begin{aligned}\alpha_T^N &= K_1^N \sqrt{\omega} + K_2^N \omega + K_3^N \omega^2 \\ &= (a_1^N + a_2^N) \sqrt{\omega} + (b_1^N + b_2^N) \omega + (d_1^N + d_2^N) \omega^2\end{aligned}\quad (8)$$

$$\begin{aligned}\alpha_T^W &= K_1^W \sqrt{\omega} + K_2^W \omega + K_3^W \omega^2 \\ &= (a_1^W + a_2^W) \sqrt{\omega} + (b_1^W + b_2^W) \omega + (d_1^W + d_2^W) \omega^2\end{aligned}\quad (9)$$

where $K_1 = a_1 + a_2$, $K_2 = b_1 + b_2$ and $K_3 = d_1 + d_2$. K_1 , K_2 and K_3 are the coefficients of the three terms in the total attenuation factor. The superscript ‘N’ means the narrow trace and the superscript ‘W’ means the wide trace. From (8) and (9), one can further obtain

$$\begin{cases} K_2^N - K_2^W = b_2^N \left(1 - \frac{b_2^W}{b_2^N} \right) \\ K_3^N - K_3^W = d_2^N \left(1 - \frac{d_2^W}{d_2^N} \right) \end{cases} \quad (10)$$

When the cross-sectional geometries and the conductor roughness information are known (which can be obtained from an Scanning Electron Microscope, SEM, measurement if needed by cutting the board and treating the cross section), the coefficient ratios can be estimated based on the physical understanding of the loss mechanisms as [38][39].

$$\begin{cases} \frac{b_2^W}{b_2^N} = \frac{P_r^N}{P_r^W} \times \frac{(A_1^W / \Lambda_1^W + A_2^W / \Lambda_2^W)}{(A_1^N / \Lambda_1^N + A_2^N / \Lambda_2^N)} \\ \frac{d_2^W}{d_2^N} = \frac{P_r^N}{P_r^W} \times \frac{(A_1^W / \Lambda_1^W + A_2^W / \Lambda_2^W)}{(A_1^N / \Lambda_1^N + A_2^N / \Lambda_2^N)} \end{cases} \quad (11)$$

where, as illustrated in Figure 1.1, P is the perimeter of the trace cross-section; A is the peak to valley amplitude of the roughness; Λ is the peak-to-peak roughness period; t is the trace thickness; and, w is the trace width. The subscript '1' is for the oxide side and '2' is for the foil side of the trace.

After removing the surface roughness effect, the dielectric attenuation factor α_D is obtained by (12) through (14). β_D is similarly obtained. When α_D and β_D are obtained, Dk and Df can be calculated by (2).

The overall flowchart of the ‘‘Root-Omega’’ method is shown in Figure 1.2.

$$\left\{ \begin{array}{l} b_2^N = \frac{K_2^N - K_2^W}{\left(1 - \frac{b_2^W}{b_2^N}\right)} \\ d_2^N = \frac{K_3^N - K_3^W}{\left(1 - \frac{d_2^W}{d_2^N}\right)} \end{array} \right. \quad (12)$$

$$\left\{ \begin{array}{l} b_1^N = b_1^W = K_2^N - b_2^N \\ d_1^N = d_1^W = K_3^N - d_2^N \end{array} \right. \quad (13)$$

$$\alpha_D = b_1^N \omega + d_1^N \omega^2 \quad (14)$$

1.1.2. Limitations. The Root-Omega method has certain limitations when extraction Dk and Df.

1.1.2.1 Dielectric property extraction for smooth conductor. Models of two stripline traces with smooth conductor different trace widths, but the same dielectric substrate were built in the HFSS as shown in Figure 1.3 and Figure 1.4. To make sure the full-wave simulations were conducted properly, the simulated results were checked in a few ways. For example, as shown in Figure 1.5, the S-parameters of two 1 inch traces were cascaded and compared with the S-parameters of 2 inch traces with the same cross section geometry. The corresponding ABCD parameters were also checked. For example, the A and D terms in the ABCD parameters are compared. They shall be the same due to symmetry.

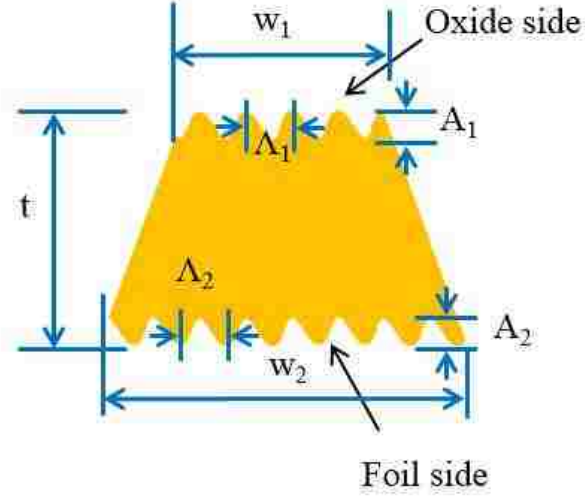


Figure 1.1. Illustration of the cross section of a rough stripline

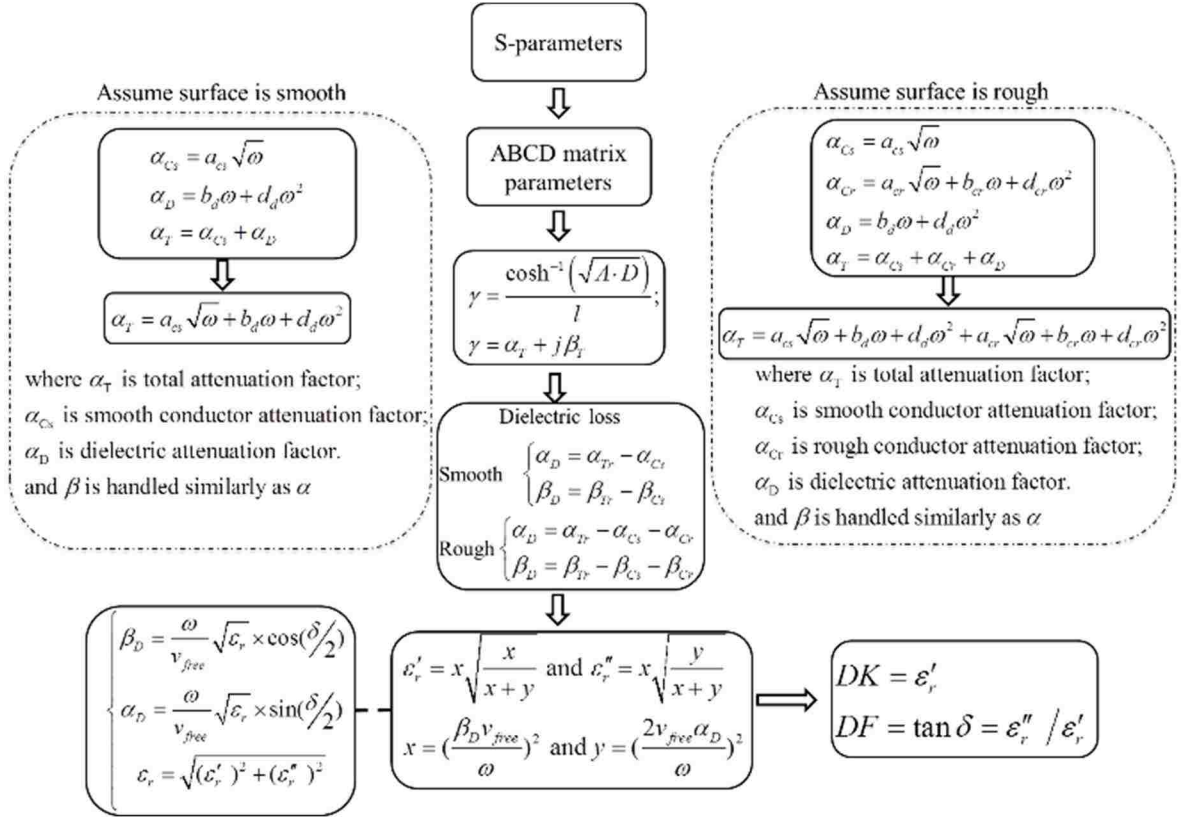


Figure 1.2. Flowchart of the “root-omega” method

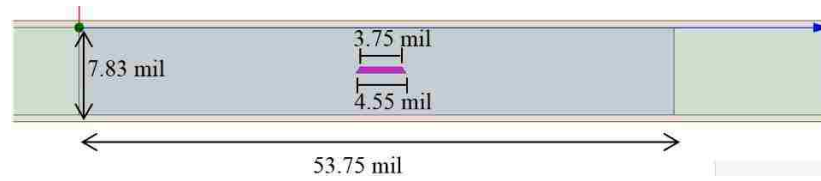


Figure 1.3. Cross section of the narrow trace

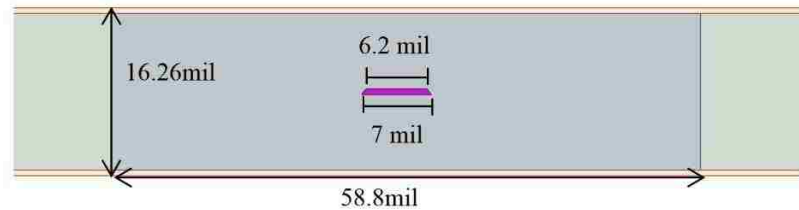


Figure 1.4. Cross section of the wide trace

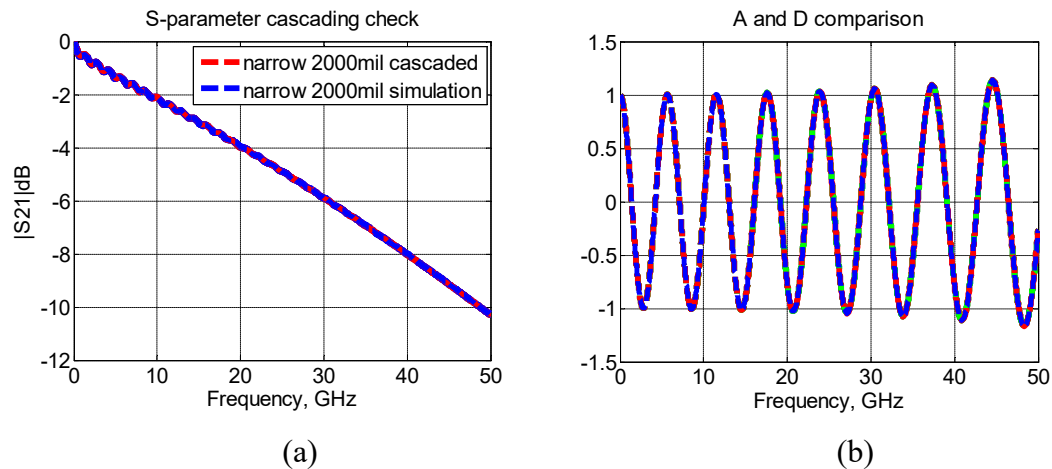


Figure 1.5. Validation of S-parameters. a) compare cascaded S-parameters with the one-piece S-parameters. b) compare cascaded A and D terms with the one-piece A and D terms, respectively

The D_k and D_f values were calculated from the simulated S-parameters. Two different dielectric materials with different D_f values were studied. For each material, traces with different trace widths and different trace lengths were simulated. The extracted values are shown and compared in Figure 1.6 and Figure 1.7. Since the conductor surface was assumed to be smooth, the trace width and trace length shouldn't affect the extracted D_k and D_f values. In other words, different trace length doesn't affect

γ values for the transmission line. Different trace width only changes conductor loss and will not contribute to the dielectric loss. The dielectric loss is determined by material properties.

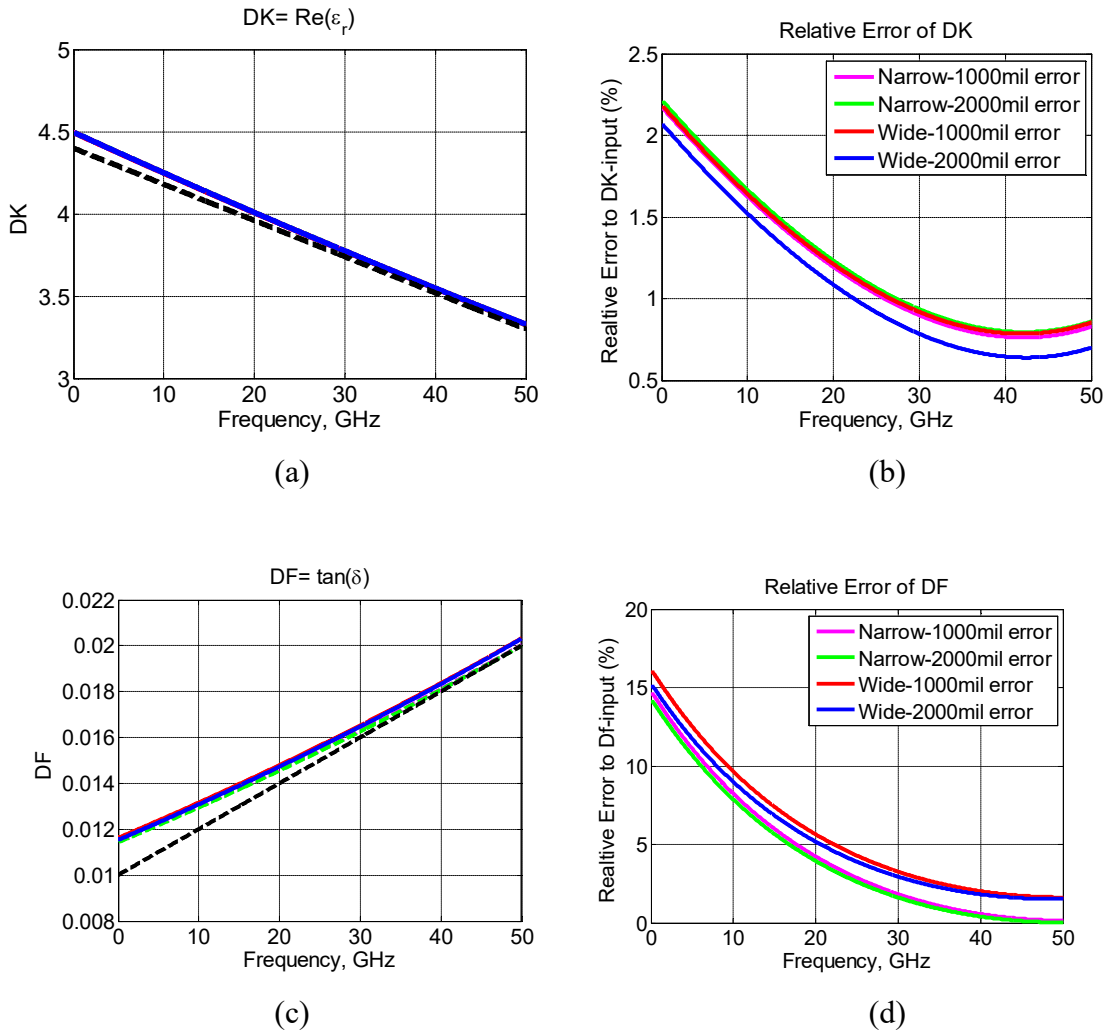


Figure 1.6. Dk and Df extraction for a large Df material

It can be seen from the figures that in general the Dk extraction works pretty well with a relative error less than 2.5% in the entire frequency band up to 50 GHz for both dielectric materials. In addition, different trace widths and lengths have little impact on the final results. The Df extraction is a different story. The extraction is better for the

large loss tangent material, although the relative error at the low frequencies is as high as 15%. For the low loss tangent material, the Df extraction is much worst with larger relative error in general. Further, different trace widths and lengths result in large differences. The simulations have demonstrated that the current Df extraction procedure in the “Root-Omega” method needs further improvement.

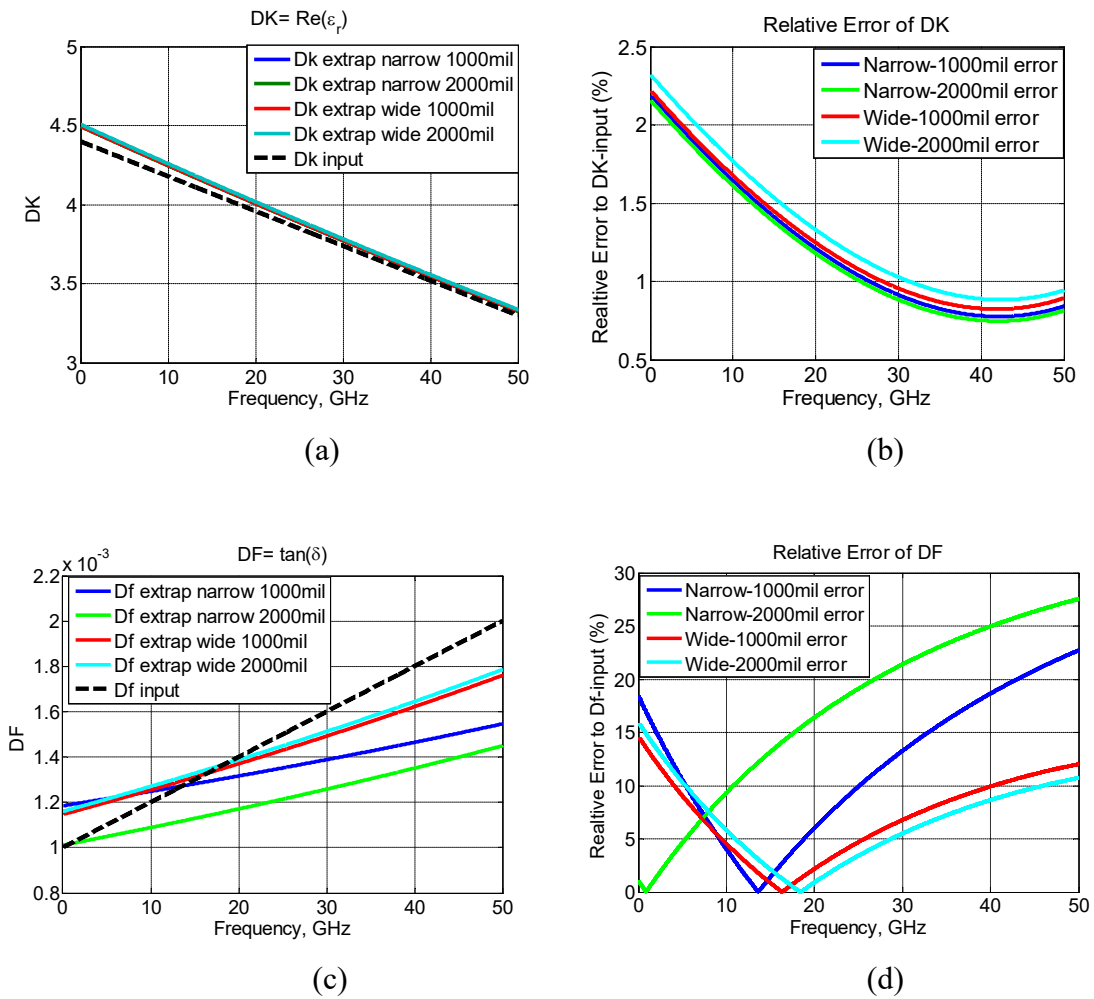


Figure 1.7. Dk and Df extraction for a small Df material

In general α_C is larger than α_D for low loss materials. When applying the curve-fitting function to extract α_D , any small error in the curve fitting procedure can result in larger error in the extracted Df value. In the Dk extraction, β_D is the dominating term in

β_T . Hence, the D_k extraction is not significantly affected by the small error in the curve fitting procedure.

Another issue for the “Root-Omega” method can be demonstrated in Figure 1.8, where the extracted D_f values are compared for the same trace but different stop frequencies were used in the extraction. It can be clearly seen that the extracted D_f values for the low loss material are not consistent, as they should be.

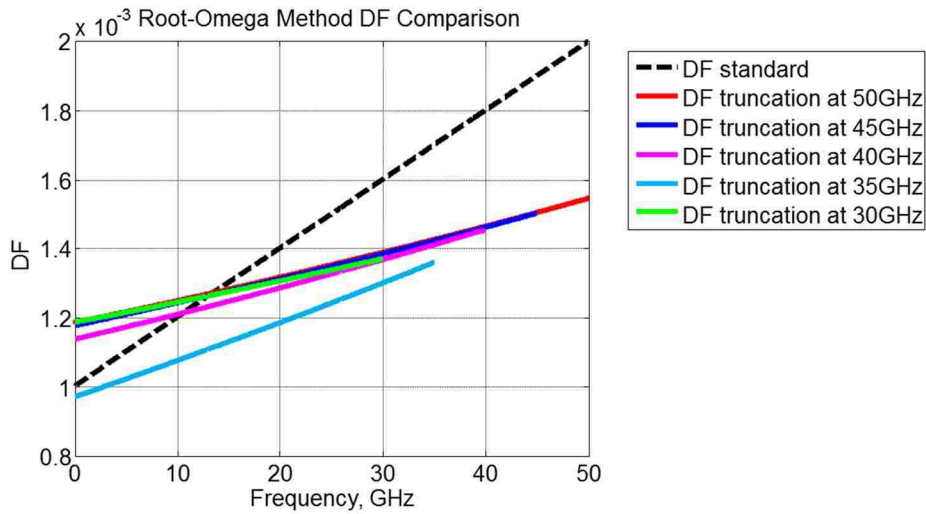


Figure 1.8. Different extracted D_f values at different frequencies

1.1.2.2 Dielectric property extraction for rough conductor. Cross sectional dimensions of two rough traces are shown in Figure 1.9 and Figure 1.10. Based on the ratios calculated from (11), D_k and D_f values were extracted and are shown in Figure 1.11 and Figure 1.12 for two dielectric materials with a large and small loss tangent, respectively. Similar conclusions can be drawn from the simulations. The D_k extraction can work well for both cases with a relative error less than 2% in the entire frequency range, while the D_f extraction needs further improvement especially for the dielectric material with a smaller loss tangent.

1.1.3. Error Sensitivity Analysis of the Root-Omega Method. It is shown that the D_k extraction has a relatively high accuracy. However, the D_f extraction has large errors, and the accuracy becomes worse for a low loss material. In this section, this

phenomenon is explained by performing the sensitivity analysis for the extracted D_k and D_f .

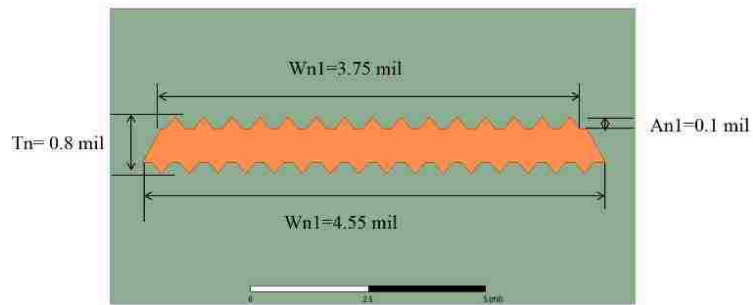


Figure 1.9. Cross section of the rough narrow trace

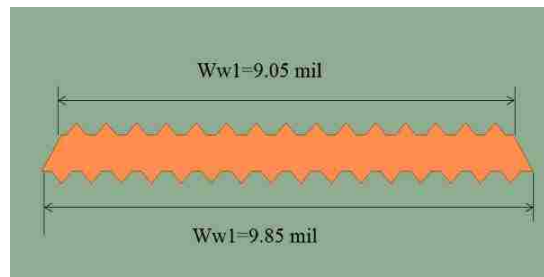


Figure 1.10. Cross section of the rough wide trace

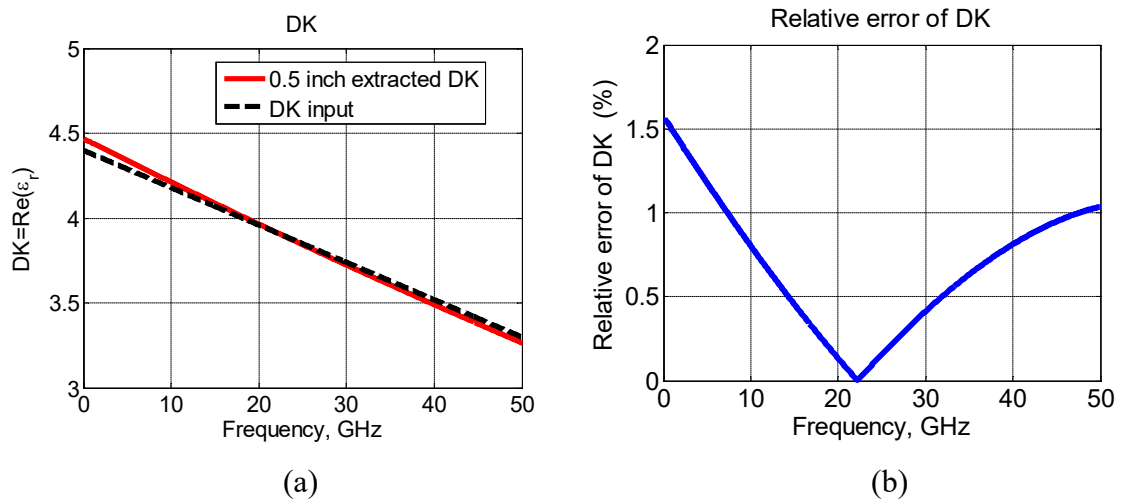


Figure 1.11. D_k and D_f extraction for a large D_f material from two rough traces

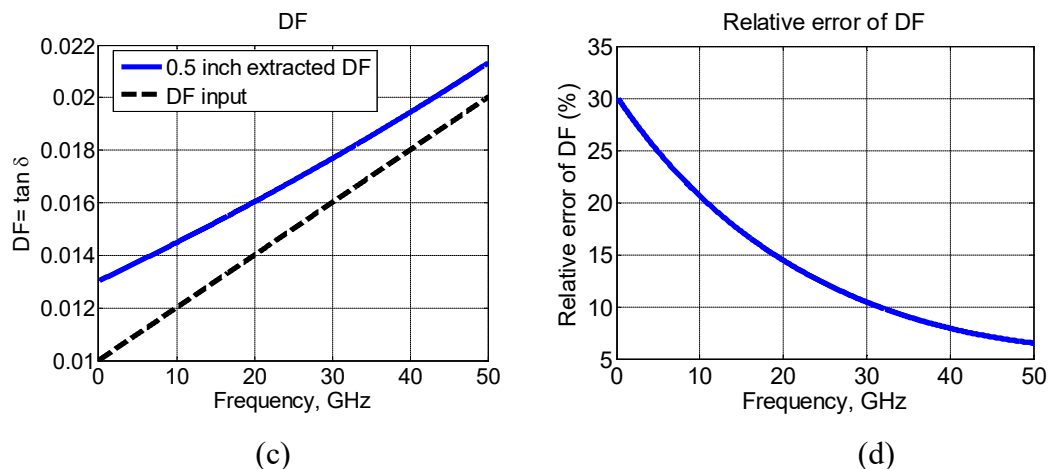


Figure 1.11. Dk and Df extraction for a large Df material from two rough traces (cont.)

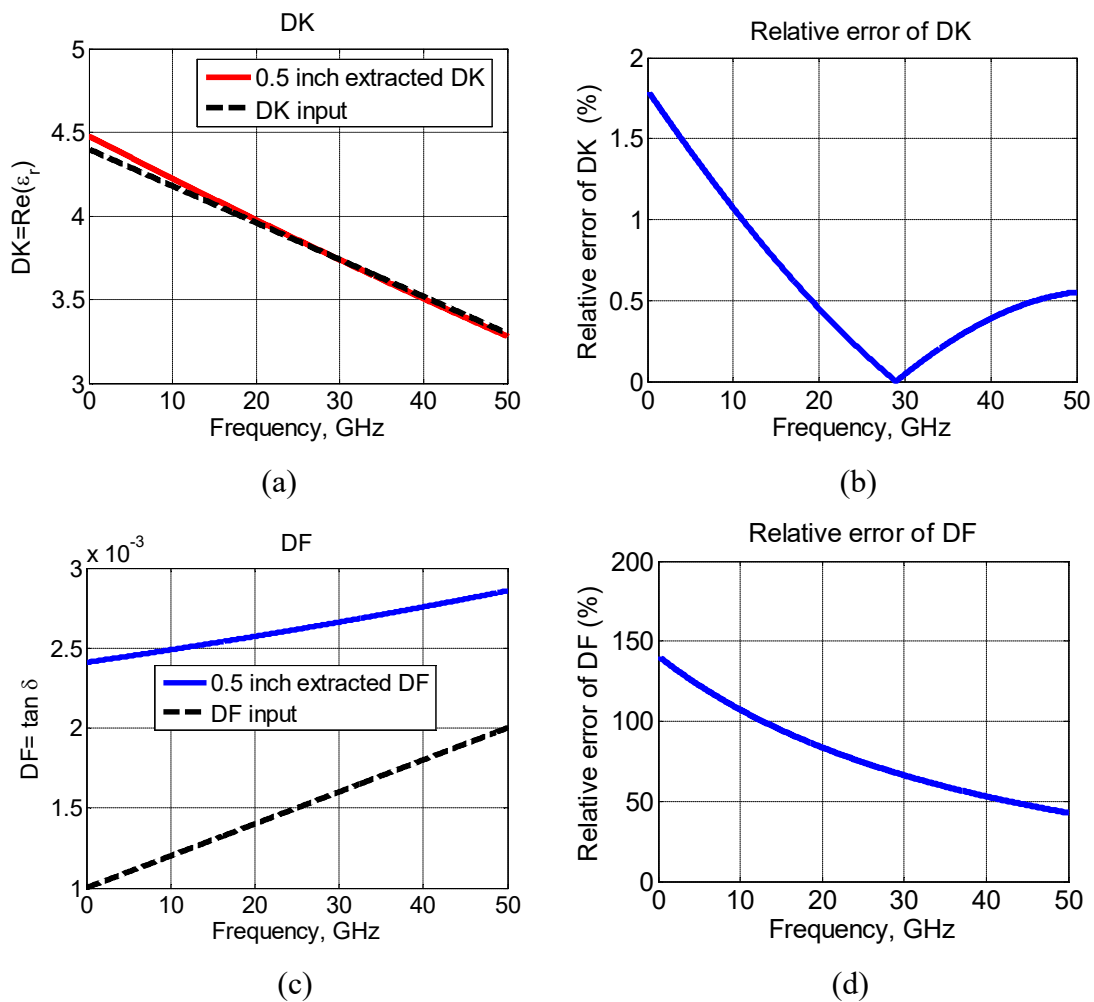


Figure 1.12. Dk and Df extraction for a small Df material from two rough traces

The Dk and Df expressions are listed here again as (15) and (16) for convenience. Then the sensitivities of Dk and Df are derived as in (17) and (18). As discussed earlier, β_D is the dominating term in β_T while α_D is not in α_T . Then, the errors generated in the curve fitting result in a large $\Delta\alpha_D$ and a small $\Delta\beta_D$. However, in (17), the coefficient of $\Delta\alpha_D$ is almost zero. Therefore, the extracted Dk is not sensitive to the curve fitting errors. In (18), however, the curve fitting errors are directly transferred to the extracted Df value. Therefore, as seen in the simulation results, the extracted Df values is very sensitive to the curve fitting errors.

$$DK = \frac{(v_{free}\beta_D)^2}{\omega^2} \sqrt{\frac{\beta_D^2}{\beta_D^2 + 4\alpha_D^2}} \quad (15)$$

$$DF = \frac{2\alpha_D}{\beta_D} \quad (16)$$

$$\frac{|\Delta DK|}{DK} = \frac{4\alpha_D}{\beta_D(\beta_D^2 + 4\alpha_D^2)^{3/2}} \Delta\alpha_D + \frac{2(\beta_D^2 + 6\alpha_D^2)}{\beta_D(\beta_D^2 + 4\alpha_D^2)} \Delta\beta_D \quad (17)$$

$$\frac{|\Delta DF|}{DF} = \frac{\Delta\alpha_D}{\alpha_D} + \frac{\Delta\beta_D}{\beta_D} \quad (18)$$

1.2. THE IMPROVED METHOD AND ERROR ANALYSIS

Improvements are proposed to address the issues discussed earlier in the original “Root-Omega” method. Again, accurate S-parameters for the transmission-line portion only of the trace(s) are required for the Dk and Df extraction. A more accurate mathematical model for α_T and β_T is developed based on the transmission-line theory for better extraction of the dielectric contributions. The equivalent Dk is then calculated first based on β_D using a new iterative procedure to achieve a higher accuracy. The equivalent Df is eventually calculated from the α_D and equivalent Dk values.

1.2.1. The Improved Root-Omega Method. The improved Root-Omega method is proposed to extract Dk and Df.

1.2.1.1 The improved root-omega method for smooth conductor. The total attenuation factor α_T and the total propagation constant β_T can be obtained from the real and the imaginary portion of the complex propagation constant γ , respectively, as

$$\begin{aligned}
 \gamma &= \sqrt{(R + j\omega L)(G + j\omega C)} \\
 &= \sqrt{RG - \omega^2 LC + j\omega(RC + GL)} \\
 &= j\omega\sqrt{LC} \sqrt{1 - \frac{RG}{\omega^2 LC} - j\frac{RC + GL}{\omega LC}} \\
 &\approx j\omega\sqrt{LC} \sqrt{1 - j\frac{RC + GL}{\omega LC}} \\
 &= \frac{1}{2} \left(\frac{RC + GL}{\sqrt{LC}} \right) + j\omega\sqrt{LC}
 \end{aligned} \tag{19}$$

where RLGC are the per-unit-length (pul) parameters of the transmission line. Since RG is far smaller than $\omega^2 LC$ and the term $\frac{RG}{\omega^2 LC}$ can be ignored. Inside the square root, $(RC+GL)$ was smaller than ωLC so Taylor's expansion was used in Eqn. (19).

$$\alpha_T = \frac{1}{2} \left(\frac{RC + GL}{\sqrt{LC}} \right) \tag{20}$$

$$\begin{aligned}
 \beta_T &= \omega\sqrt{LC} \\
 &= \omega\sqrt{(L_e + L_i)C} \\
 &= \omega\sqrt{L_e C} \sqrt{1 + \frac{L_i}{L_e}} \\
 &\approx \omega\sqrt{L_e C} \left(1 + \frac{L_i}{2L_e} \right) \text{ where } \left(\frac{L_i}{L_e} \ll 1 \right) \\
 &= \frac{\omega L_i}{2} \sqrt{\frac{C}{L_e}} + \omega\sqrt{L_e C}
 \end{aligned} \tag{21}$$

The conductor loss α_C and the dielectric loss α_D are approximated in (22) and (23) for low loss cases, as the conductor loss α_C due to the skin effect is related to R and the dielectric loss α_D is related to G.

$$\alpha_C = \frac{1}{2} R \sqrt{\frac{C}{L}} \quad (22)$$

$$\alpha_D = \frac{1}{2} G \sqrt{\frac{L}{C}} \quad (23)$$

The conductor propagation constant β_C and dielectric propagation constant β_D are expressed in (24) and (25). It is known that the pul inductance is the summation of internal and external inductances. And the internal inductance is small compared with the external inductance. Taylor expansion is used to separate β_C which is due to the skin effect and β_D . In (24), Wheeler's incremental inductance rule is applied.

$$\begin{aligned} \beta_C &= \frac{\omega L_i}{2} \sqrt{\frac{C}{L_e}} \\ &= \frac{R}{2} \sqrt{\frac{C}{L_e}} \end{aligned} \quad (24)$$

$$\beta_D = \omega \sqrt{L_e C} \quad (25)$$

where L_i and L_e are the pul internal and external inductances, respectively.

Also R due to skin effect is proportional to the $\sqrt{\omega}$ and C is proportional to the dielectric constant (Dk); therefore, the conductor loss α_C in (22) can be represented in terms of ω and Dk as in (26). It is proportional to $\sqrt{\omega}$ and \sqrt{Dk} . For dielectric loss α_D , G is proportional to frequency and loss tangent (Df) when an equivalent homogeneous medium is assumed. So the dielectric loss α_D in (23) can be represented as in (27). Since the dielectric constant and loss tangent can be reasonably assumed to be a frequency-dependent linear line due to the nature of materials. Therefore, the dielectric attenuation

factor α_D in (27) can be represented as (28). In other words, α_D is proportional to ω , ω^2 and \sqrt{Dk} .

$$\alpha_C = a\sqrt{\omega}\sqrt{DK} \quad (26)$$

$$\alpha_D = \frac{1}{2}\omega \frac{\sqrt{DK}}{v_{free}} DF \quad (27)$$

$$\alpha_D = (b\omega + d\omega^2)\sqrt{DK} \quad (28)$$

where a , b , d are the unknown coefficients.

Similarly, β_C and β_D can be rewritten as in (29) and (30), respectively. β_C is proportional to $\sqrt{\omega}$ and \sqrt{Dk} . β_D is proportional to ω and \sqrt{Dk} . Compared with the original ‘‘Root-Omega’’ method, β_D doesn’t have ω^2 terms.

$$\beta_C = k\sqrt{\omega}\sqrt{DK} \quad (29)$$

$$\beta_D = \frac{\omega}{v_{free}}\sqrt{DK} \quad (30)$$

where k is the unknown coefficient.

From the theoretical derivations, the \sqrt{Dk} term should be considered in both α_T and β_T , which were not included in the original ‘‘Root-Omega’’ method. This is found to be one of the main reasons for the accuracy and consistency issues demonstrated earlier. And the ω^2 term is incorrectly considered in the original ‘‘Root-Omega’’ method for β_D . The mathematical models for α_T and β_T in the improved ‘‘Root-Omega’’ method are proposed as (31) and (32). The equivalent Dk can be calculated first based on β_D in (30) and then the equivalent Df from α_D in (27), as described in (34).

$$\alpha_T = (a\sqrt{\omega} + b\omega + d\omega^2)\sqrt{DK} \quad (31)$$

$$\beta_T = \left(k\sqrt{\omega} + \frac{\omega}{v_{free}} \right) \sqrt{DK} \quad (32)$$

$$DK = \left(\frac{\beta_D v_{free}}{\omega} \right)^2, \quad (33)$$

$$DF = \frac{2v_{free}\alpha_D}{\sqrt{DK}}, \quad (34)$$

where a , b , d and k are the unknown coefficients, which will be obtained through curve-fitting.

In the mathematical model, there is only one unknown coefficient k in β_T so it would be more accurate to fit for Dk values from β_T instead of α_T because the less the number of unknowns in the fitting the more accurate the fitted values are. Since the Dk is in the square root format in the β_T and cannot be fitted by the least square method directly, an iterative procedure is developed, which actually further improves the accuracy of the Dk extraction. A rough initial value for Dk is needed to start the iteration process. The flowchart of the detailed procedures in the improved ‘‘Root-Omega’’ method for smooth conductor is shown in Figure 1.13. In Step 1, β_T is divided by ω in order to increase the weight for the low frequency band in the curve fitting and improve accuracy. After that, it is fitted with terms of one over $\sqrt{\omega}$, a constant unknown and ω for coefficients k_1 , k_2 , and k_3 so the initial β_D is obtained. In Step 2, the initial rough Dk is calculated from the mathematical model of β_D . The Dk values need to be corrected from the initial rough values. In Step 3, an iteration calculation procedure is used to correct the Dk values and a correction term ΔDk is obtained. If ΔDk is smaller than a defined tolerance, the Dk values are deemed converged, otherwise another iteration is conducted until the Dk values converge. In Step 4, α_D is fitted with the \sqrt{Dk} considered. In step 5, the Df values are obtained by (34).

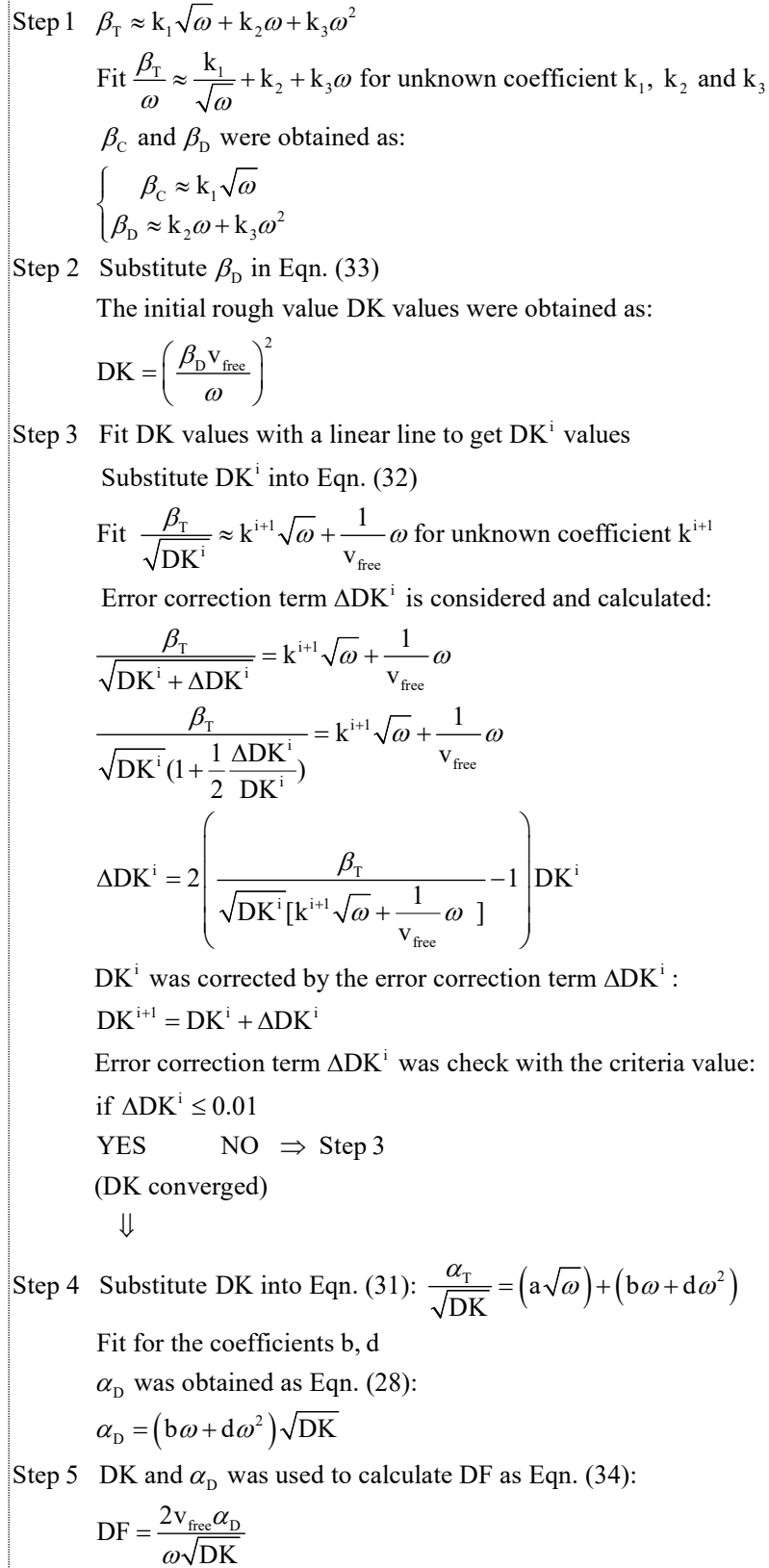


Figure 1.13. The procedure of Dk and Df extraction for smooth conductor

1.2.1.2 The improved root-omega method for rough conductor. When the conductor is rough, the total attenuation factor α_T and total propagation constant β_T have conductor contribution, dielectric contribution and roughness contribution. In the previous subsection, the attenuation factor and propagation constant for smooth conductor are obtained. The rough conductor contributions have a similar frequency dependency, as shown in (35) and (36). Thus, the total attenuation factor α_T and total propagation constant β_T of the rough conductor can be written as in (37) and (38).

$$\alpha_{cr} = \left(a_{cr} \sqrt{\omega} + b_{cr} \omega + d_{cr} \omega^2 \right) \sqrt{DK} \quad (35)$$

$$\beta_{cr} = \left(a'_{cr} \sqrt{\omega} + b'_{cr} \omega + d'_{cr} \omega^2 \right) \sqrt{DK} \quad (36)$$

$$\begin{aligned} \alpha_T &= \alpha_{C0} + \alpha_D + \alpha_{Cr} \\ &= \left(a_{cs} \sqrt{\omega} \sqrt{DK} \right) + \left(\left(b_d \omega + d_d \omega^2 \right) \sqrt{DK} \right) \\ &\quad + \left(\left(a_{cr} \sqrt{\omega} + b_{cr} \omega + d_{cr} \omega^2 \right) \sqrt{DK} \right) \\ &= \left[\left(a_{cs} + a_{cr} \right) \sqrt{\omega} + \left(b_{cr} + b_d \right) \omega + \left(d_{cr} + d_d \right) \omega^2 \right] \sqrt{DK} \end{aligned} \quad (37)$$

where a_{cs} is the coefficient of smooth conductor attenuation factor; d_d is the coefficient of dielectric conductor attenuation factor; a_{cr} , b_{cr} and d_{cr} are coefficients of rough conductor attenuation factor.

$$\beta_T = \left[\left(a'_{cs} + a'_{cr} \right) \sqrt{\omega} + \left(\frac{1}{v_{free}} + b'_{cr} \right) \omega + d'_{cr} \omega^2 \right] \sqrt{DK} \quad (38)$$

where a'_{cs} is the coefficient of the smooth conductor propagation constant; a'_{cr} , b'_{cr} and d'_{dr} are coefficients of the rough conductor propagation constant.

Similar as in the original ‘‘Root-Omerga’’ method, two striplines are need to eliminate the roughness contribution.

The flowchart of the improved “Root-Omega” method with an iterative procedure for rough conductor is shown in Figure 1.14. In Step 1, the initial rough D_k values are calculated from β_T using the original “Root-Omega” method with known cross section and roughness information. The D_k values obtained at the k^{th} step are fitted with frequency dependent linear lines in Step 2 [29]. In Steps 3 and 4, β_T is divided by the square root of the fitted k^{th} -step D_k values and fitted for β_D with cross section information. In step 5, the $(k+1)^{\text{th}}$ -step D_k values are calculated by (33). In step 6, if the difference between the k^{th} -step and $(k+1)^{\text{th}}$ -step D_k values is smaller than a defined tolerance, the D_k extraction is deemed converged; otherwise, Step 2 to Step 6 are performed again. In steps 7 and 8, when the D_k values are converged, α_T divided by $\sqrt{D_k}$ and ω is fitted for α_D with cross-section information. In step 9, D_f values are calculated by (34). The overall flowchart of the improved “Root-Omega” method is shown in Figure 1.15.

1.2.2. Validation of the Improved Root-Omega Method. The proposed method is validated the relative error for D_k and D_f is reduced.

1.2.2.1 Dielectric property extraction. Two smooth stripline traces with different widths, but the same low loss dielectric medium were built in the 2D simulation as shown in Figure 1.16. The D_k and D_f values were calculated from the simulated S-parameters. The extracted values are compared in Figure 1.17 and Figure 1.18. Since the conductor surface was assumed to be smooth, the trace width and length didn’t affect the extracted D_k and D_f values. The extracted D_k and D_f values were compared with the input values and the relative errors between extracted values and the input values were shown in Figure 1.17 and Figure 1.18.

From the figures, in general the D_k and D_f extraction works pretty well with a relative error less than 0.03% and 2%, respectively, in the entire frequency band up to 50 GHz. The simulations demonstrated that the improved “Root-Omega” method increased the accuracy of D_k and D_f extraction for low-loss material. And also the extracted D_f values are consistent with different stop frequencies, as shown in Figure 1.19.

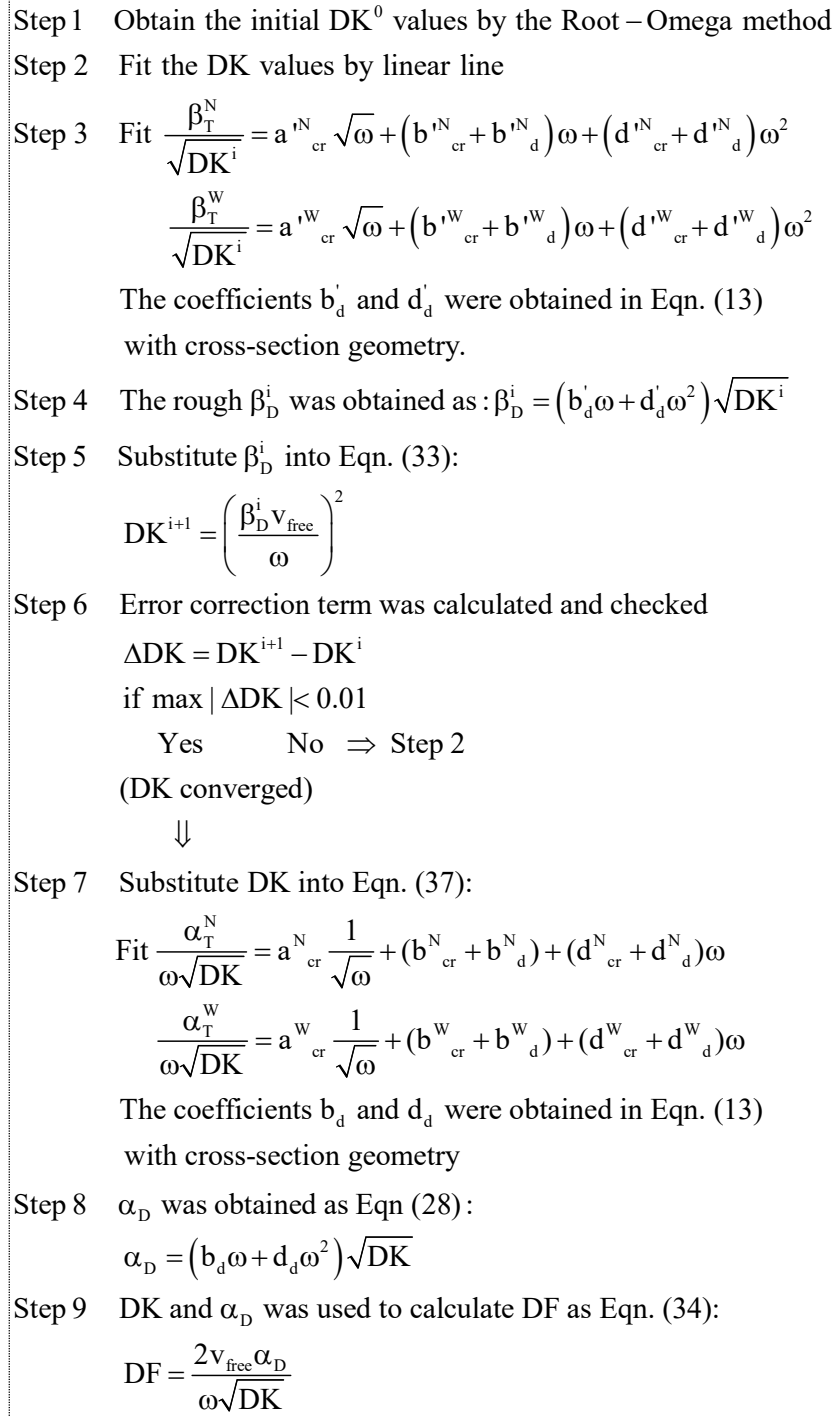


Figure 1.14. The procedure of Dk and Df extraction for rough conductor

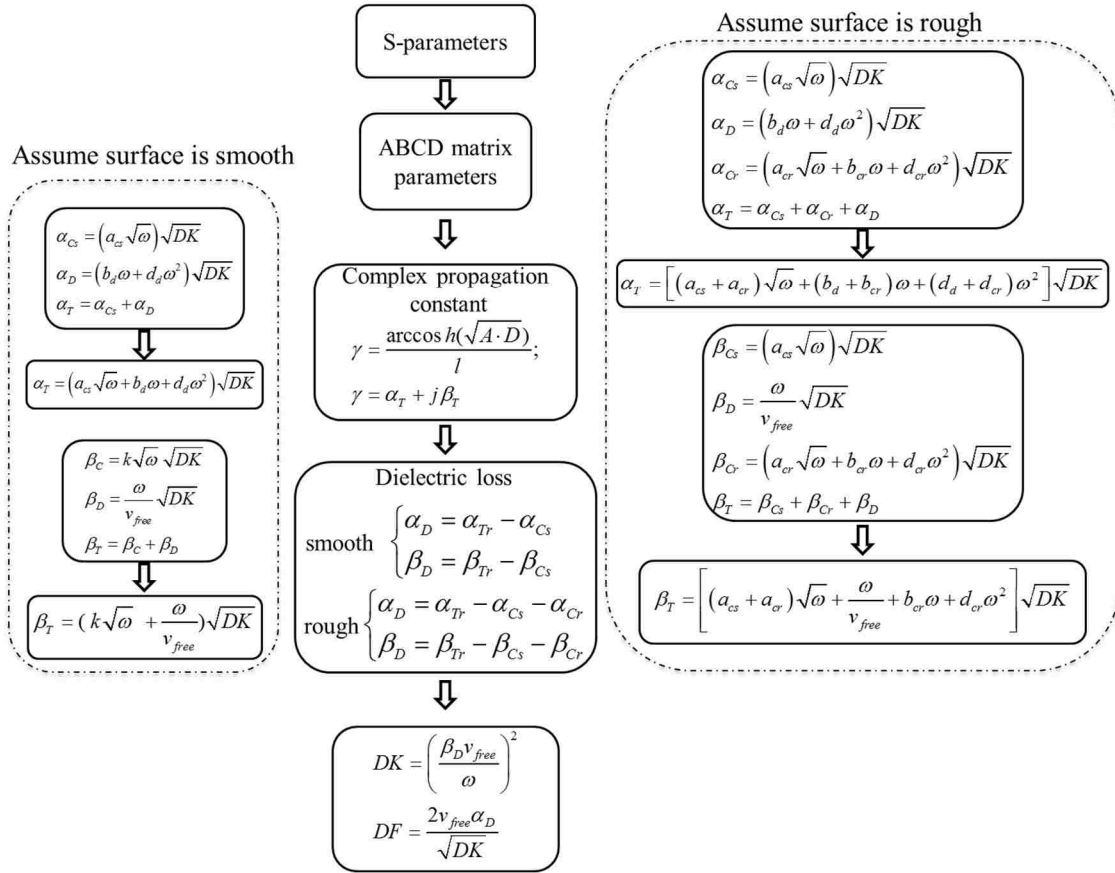


Figure 1.15. Flowchart of the improved “Root-omega” method

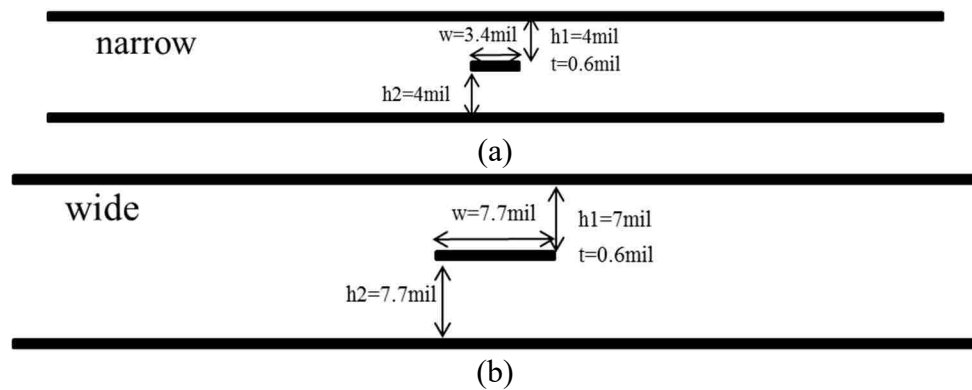


Figure 1.16. Illustration of the cross section of two smooth striplines. (a) narrow smooth trace (b) wide smooth trace

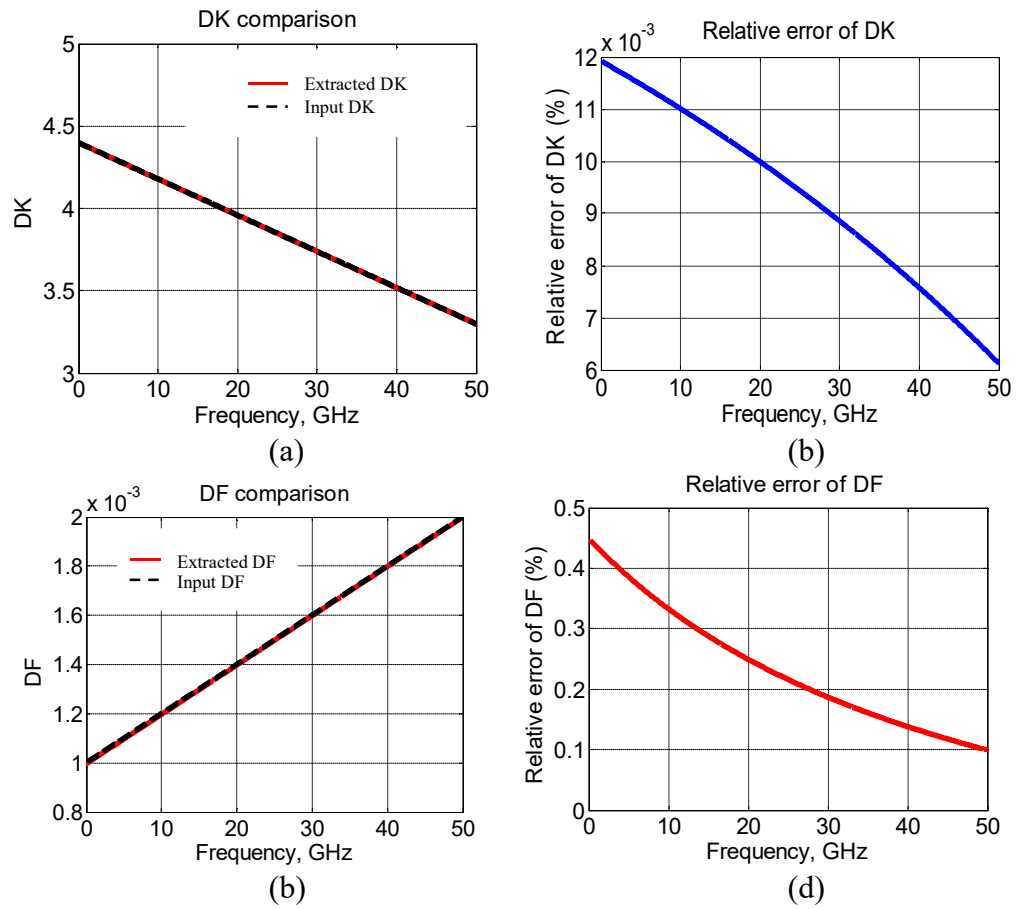


Figure 1.17. Validation of extracted Dk and Df in wide trace. (a) Dk comparison (b) relative error of extraction Dk to standard values (c) Df comparison (d) relative error of extracted Df to standard values

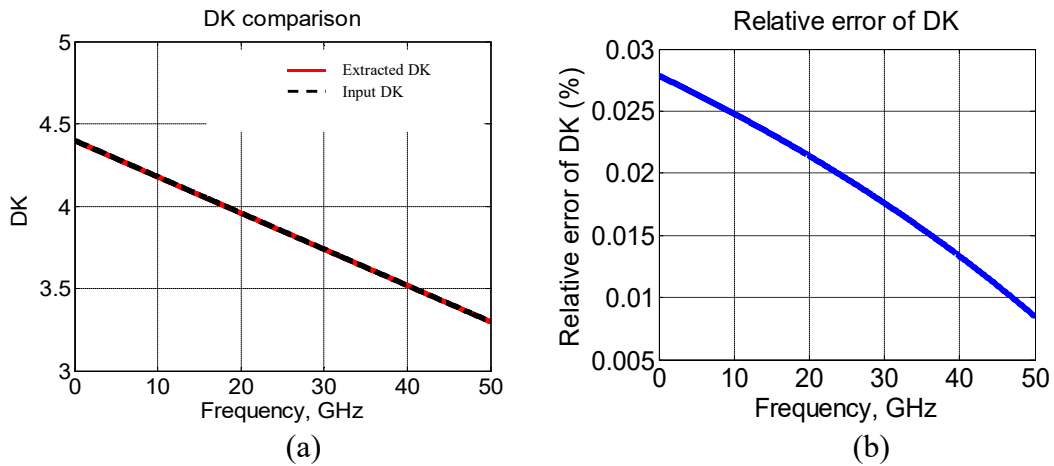


Figure 1.18. Validation of extracted Dk and Df in narrow trace

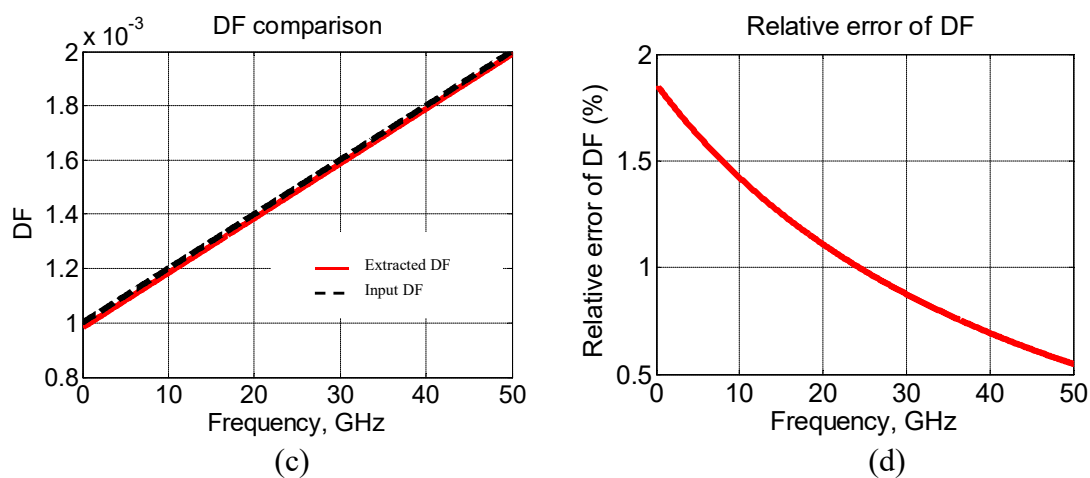


Figure 1.18. Validation of extracted Dk and Df in narrow trace (cont.)

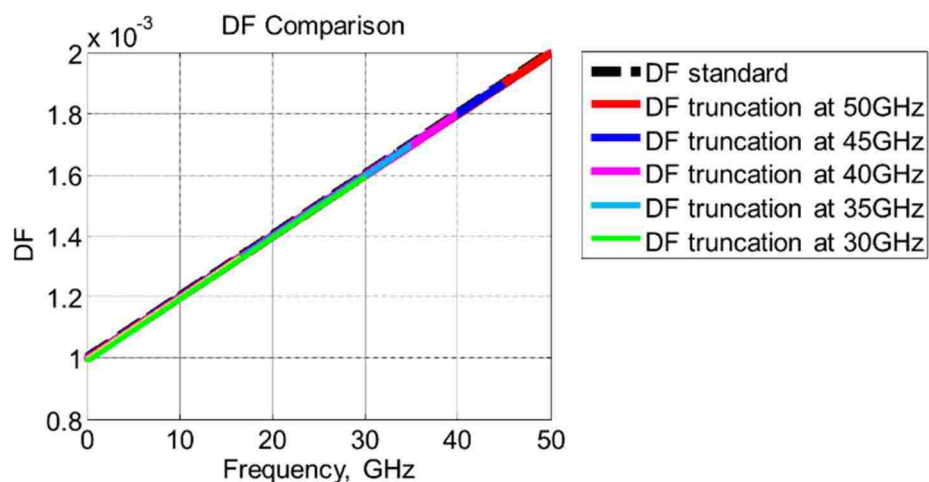


Figure 1.19 Extracted DF with different cut frequency

1.2.2.2 Dielectric property extraction for rough conductor. Cross sectional dimensions of two rough traces are shown in Figure 1.20. Dk and Df values were extracted and are shown in Figure 1.21. Similar conclusions can be drawn from the simulations. The Dk and Df extraction can work well with a relative error less than 0.01% and 6%, respectively, in the entire frequency range.

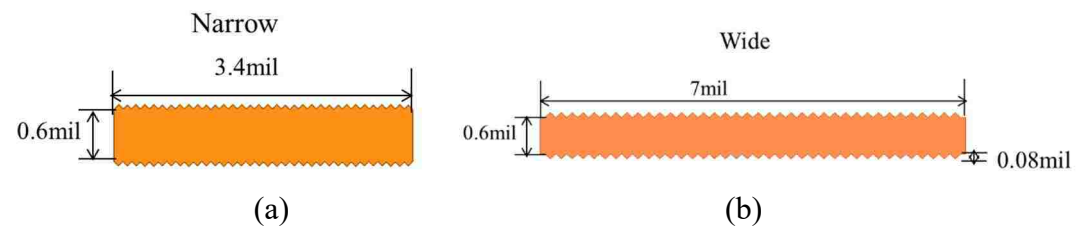


Figure 1.20. Illustration of the cross section of two rough stripline. (a) narrow trace stripline (b) wide trace stripline

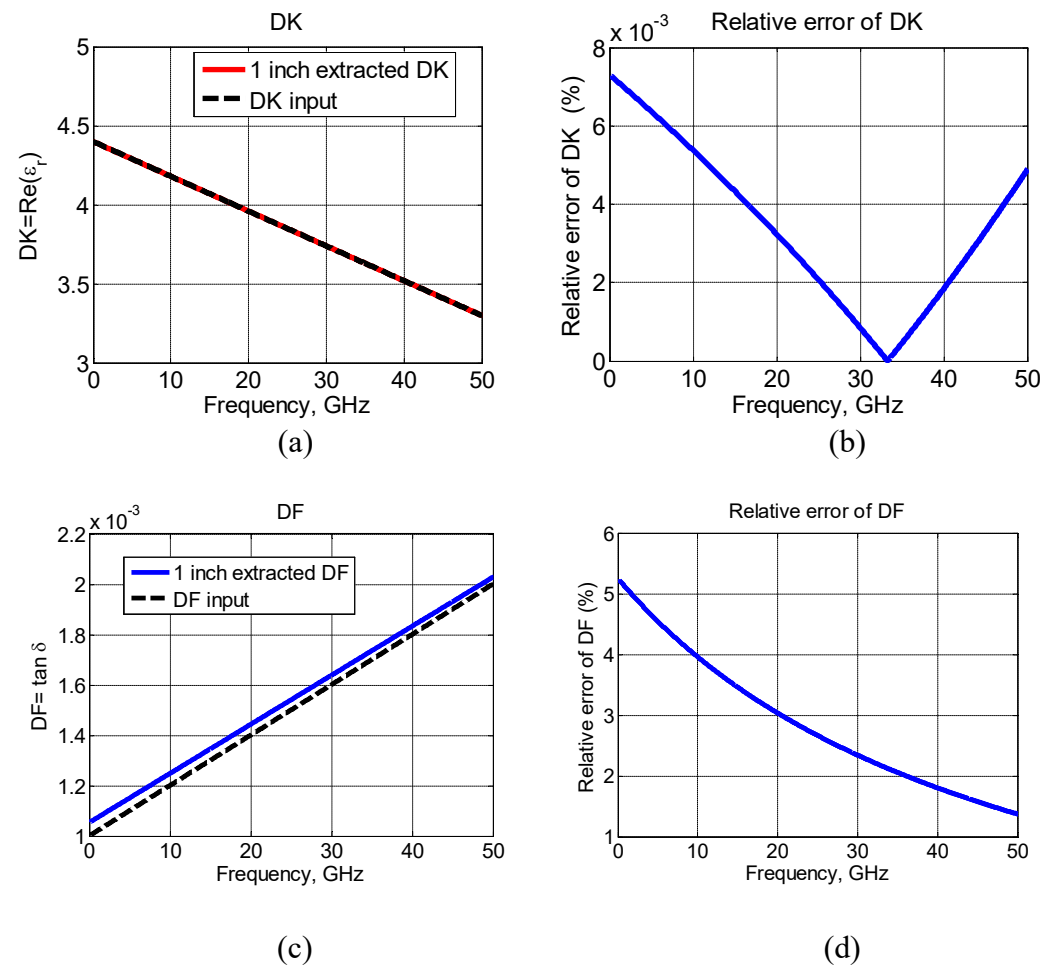


Figure 1.21. Validation of extracted Dk and Df in rough trace. (a) Dk comparison (b) relative error of extraction Dk to standard values (c) Df comparison (d) relative error of extracted Df to standard values

Another validation case was demonstrated with a simulation model of the Huray roughness factor. The Huray roughness factor settings and geometry information are shown in Table 1.1 and Figure 1.22, respectively. The ratio of P_r^N/P_r^W is equal to the ratio of K_A^W/K_A^N since they are due to skin effect. Because the Huray factor for narrow and wide traces is the same, the coefficient ratio of b^W over b^N and ratio of d^W over d^N in the equation (12) are equal to K_A^W/K_A^N . By the improved “Root-Omega” method, Dk and Df values were extracted and are shown in Figure 1.23. The Dk and Df extraction can work well with a relative error less than 0.2% and 2.2%, respectively, in the entire frequency range.

Table 1.1. Huray roughness model settings

Nodule Radius	0.5 um
Hall Huray Surface Ratio	3.0159

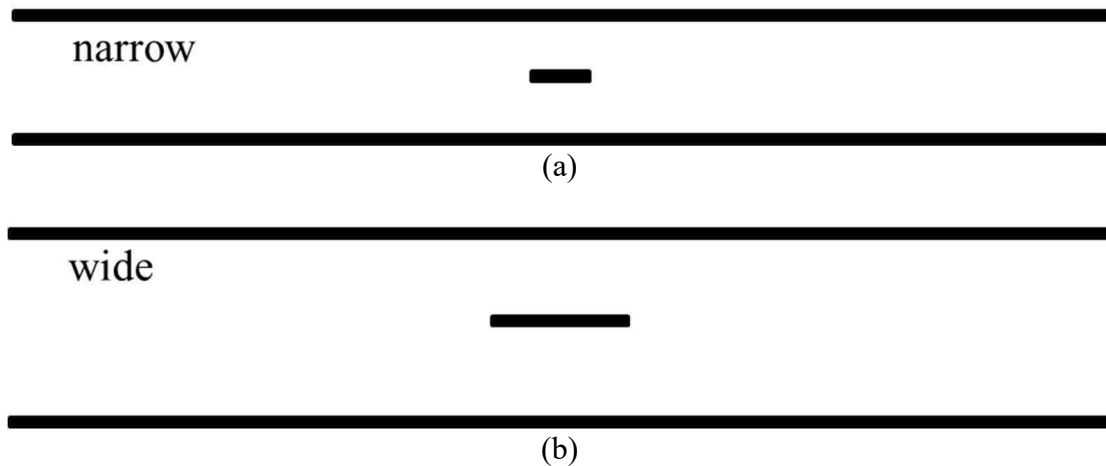


Figure 1.22. Cross section geometry of narrow and wide trace. (a) narrow trace width: 4 mil, trace thickness: 0.6 mil (b) wide trace width: 7 mil, trace thickness: 0.6 mil

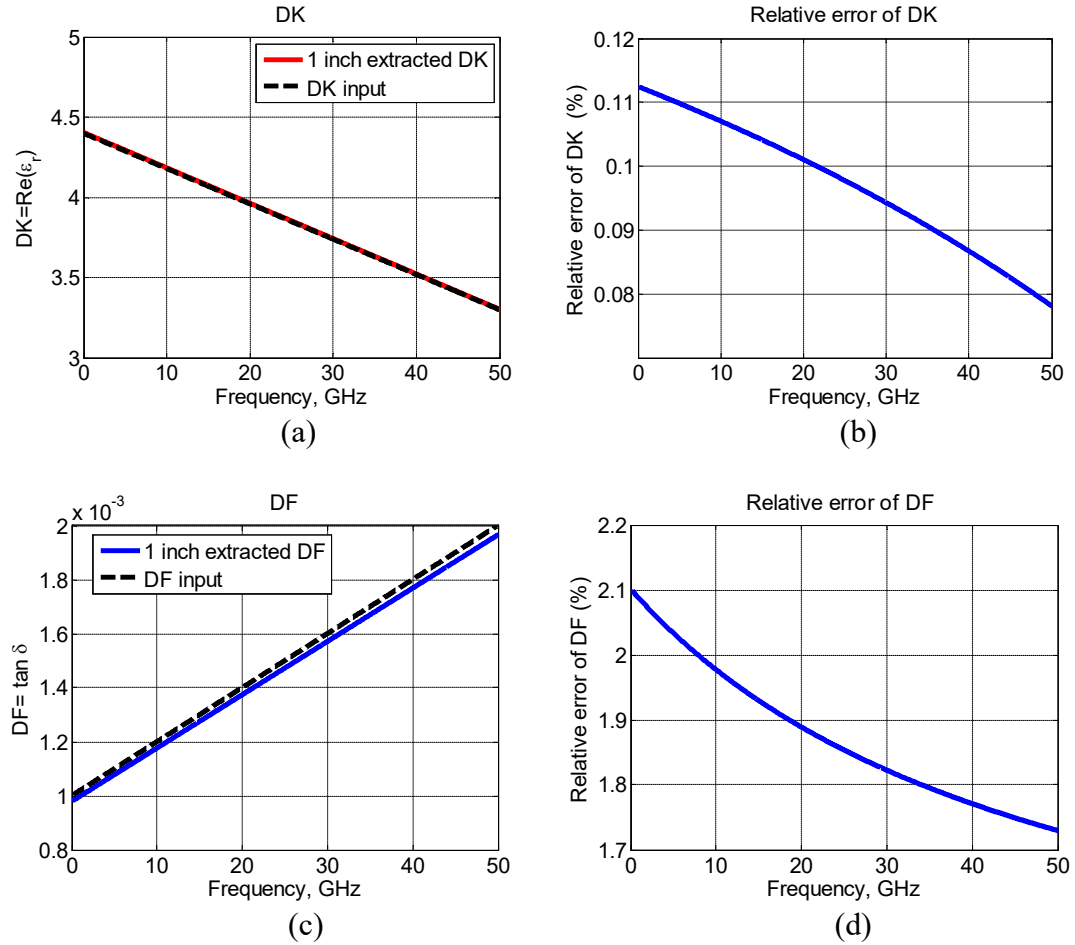


Figure 1.23. Validation of extracted Dk and Df in rough trace. (a) Dk comparison (b) relative error of extraction Dk to standard values (c) Df comparison (d) relative error of extracted Df to standard values

1.2.3. Error Sensitivity Analysis of the Improved Root-Omega Method. The Dk and Df expressions for the improved “Root-Omega” method were listed here again as (39) and (40) for convenience. The error sensitivities of Dk and Df are derived as in (41) and (42). In addition to the previous argument that $\Delta\beta_D$ is much smaller than $\Delta\alpha_D$, the additional \sqrt{DK} term and the iterative procedures introduced in the improved extraction procedure further reduce both $\Delta\alpha_D$ and $\Delta\beta_D$. Thus, the sensitivities of Dk and Df in the improved “Root-Omega” method are significantly improved.

$$DK = \left(\beta_D \frac{v_{free}}{\omega} \right)^2 \quad (39)$$

$$DF = \frac{2v_{free}\alpha_D}{\omega\sqrt{DK}} = \frac{2\alpha_D}{\beta_D} \quad (40)$$

$$\frac{|\Delta DK|}{DK} = \Delta\beta_D \frac{2}{\beta_D} \quad (41)$$

$$\frac{|\Delta DF|}{DF} = \frac{\Delta\alpha_D}{\alpha_D} + \frac{\Delta\beta_D}{\beta_D} \quad (42)$$

The improved “Root-Omega” method for the dielectric property extraction for fabricated PCB materials from transmission line S-parameters was proposed in this paper for both cases with smooth and rough conductors. Mathematical models for α_T and β_T were developed in the improved “Root-Omega” method and iteration procedure was applied to improve the accuracy of Dk and Df extraction. The algorithm works for low loss material property extraction and accuracy of the extracted Dk and Df was good with a relative error no more than a few percent in the frequency band up to 50 GHz. The consistence of the extracted Df values was ensured at different stop frequencies. Error sensitivity analysis was also performed to explain the improved accuracy of Dk and Df in the proposed algorithm.

2. MODAL BASED BGA MODELING

Digital systems are in the direction of higher data rate, higher density of integrated circuit and larger number of input/output data communications [40][41]. The channel transmitting high speed signal requires low loss material [42]-[44] and smooth transition [43]-[45]. More interconnection pins for connecting from package to printed circuit board (PCB) are required for high performance ASIC devices. Ball grid arrays (BGAs) instead of lead frame are widely used in low-cost high volume package assemblies for the extremely high pin-out density. The BGA structure needs to be carefully considered since the discontinuities may distort the TEM wave from transmission lines and may result in signal integrity issues or EMI issue which limit the system performance[46]-[50]. Hence, the thorough electrical modeling of BGA structure is a prerequisite for effective package design at the beginning of the design cycle.

Variant methods can be used for BGA modeling. BGA structure are treated as cylinders in [44][51]. Three dimensional full-wave methods are used including finite difference time domain (FDTD) approaches [51][52] and the partial element equivalent circuit (PEEC) method [53]-[55]. The modeling from numerical methods requests large number of mesh to achieve sufficient accuracy which takes long computational time. Full-wave simulation based methods are also introduced in [56]-[60]. The parasitic capacitance and inductance are extracted from the three-dimensional full-wave simulations. An equivalent circuit is built with the lumped elements. The feature selective validation procedure is good for validation between constructed model and full-wave simulations [61]-0. Based on full-wave simulations, statistical methods can be used to estimate crosstalk in the BGA structures [64]-[66]. Measurement are also used to extract lumped circuit model in [67]-[69]. S-parameters are measured from vector network analyzer. Parasitic capacitance and inductance are obtained on the measured S-parameters and the lumped element circuit model is established. A combination of simulation and measurement is also used to model BGA structures [70][71]. These circuit models works only for the specific structure simulated or measured and it is time consuming to do the simulation or measurement. And since the BGA balls are placed close to each other the current density is not ever uniformly distributed. However, these

methodologies don't consider the proximity effect when high density of BGA structure is presented.

A fast modal-based approach is proposed to extract partial inductance for BGA structures. The proximity effect is considered in the proposed methodology. Also the image theory is applied to convert the BGA structures from 3D to a 2D problem when extracting the modal-based inductance. The physical loop inductance is obtained from the proposed matrix reduction approach. Analytical solutions are obtained so that there are no singularity issues. Mesh is not required in the proposed methodology and the size of computational matrix is reduced due to the orthogonal property of modal basis functions so that the computational time is greatly reduced.

2.1. METHODOLOGY OF EQUIVALENT INDUCTANCE CALCULATION

BGA balls are placed between two ground planes, one in package and the other in PCB, shown in Figure 2.1. The balls are approximated as cylinders instead of spheres. The current direction through BGA balls is perpendicular to the two parallel plates. Assuming the two ground planes are large enough, the structure can be treated as infinitely long BGA balls by image theory, as Figure 2.2. Since there is no variation along axial direction and the 3D problem is converted to 2D problem.

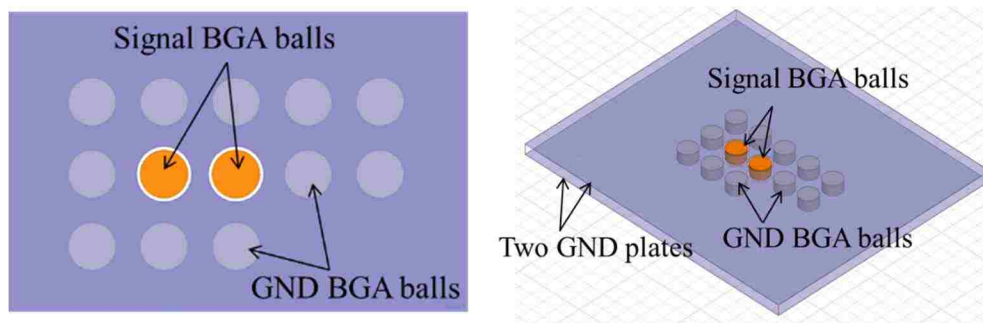


Figure 2.1. The signal and ground BGA balls are in between two parallel plates

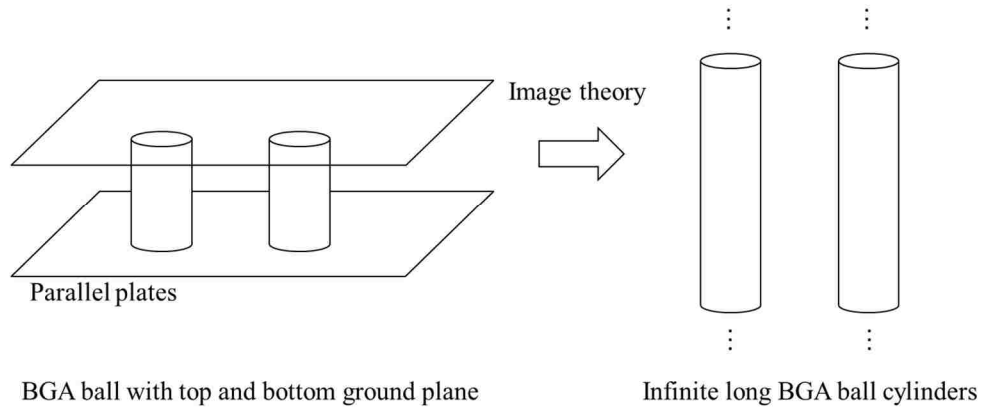


Figure 2.2. The BGA balls between two parallel plates

2.1.1. Basis Functions. BGA balls in the package are designed to be of high density with small pitch size. Since the current flowing along BGA balls are not uniformly distributed, the proximity effect should be carefully taken into consideration when modeling BGA ball structure. Assume the BGA balls are perfect electric conductor so all the current flows along the edge of the BGA balls. Considering Fourier Series can represent for any periodic function, current density can be expanded by two orthogonal basis functions and is expressed as a summation of modal current densities:

$$J^j(\vec{\rho}') = \sum_{k=1}^M a_k^j f_k^j(\vec{\rho}') \quad (1)$$

where a_k^j is the unknown modal current density and f_k^j is the basis function.

$$f_k^j = \begin{cases} 1, & k=1 \text{ (zero order mode)} \\ \cos\left(\frac{k}{2}\theta_j\right), & k > 1 \text{ \& even (higher order mode)} \\ \sin\left(\frac{k-1}{2}\theta_j\right), & k > 1 \text{ \& odd (higher order mode)} \end{cases} \quad (2)$$

The j, k are the index of the conductor and basis function, respectively. M is the total number of basis function. The angle θ_j is defined in local coordinate centered at conductor j .

The zero order basis function represents for the current uniformly distributed around the circumference of the conductor. The higher order basis functions count for the proximity effect of the current distribution by sinusoidal variation along the angular direction.

2.1.2. Modal Based Partial Inductance. The magnetic potential at arbitrary point p is contributed by all current flowing along the conductor. In the global cylindrical coordinate system the magnetic potential is expressed as

$$A(\vec{\rho}) = \sum_{j=1}^N \int_{S_j} J^j(\vec{\rho}') G^A(\vec{\rho}, \vec{\rho}') d\vec{\rho}' \quad (3)$$

where $\vec{\rho}$ and $\vec{\rho}'$ are the observation location and source location. N is the total number of conductors. G^A is the Green's function for magnetic potential in homogeneous medium. Substituting (1) into (3) results in

$$A(\vec{\rho}) = \sum_{j=1}^N \sum_{k=1}^M \int_{S_j} a_k^j f_k^j(\vec{\rho}') G^A(\vec{\rho}, \vec{\rho}') d\vec{\rho}' \quad (4)$$

Since the BGA ball structure is treated as 2D problem the Green's function for the magnetic potential in (4) is:

$$G^A(\vec{\rho}, \vec{\rho}') = \frac{\mu}{4\pi} \ln \frac{1}{|\vec{\rho} - \vec{\rho}'|^2} \quad (5)$$

Magnetic flux wrapping the i th ball is defined as:

$$\Psi_i = \int_{S_i} A \cdot dl \quad (6)$$

Substitute (4) into (6):

$$\Psi_i = h \sum_{j=1}^N \sum_{k=1}^M a_k^j \int_{S_j} f_k^j(\vec{\rho}') G^A(\vec{\rho}, \vec{\rho}') d\vec{\rho}' \quad (7)$$

where h is the length of the conductor.

Let's define

$$\psi_k^j(\vec{\rho}) = h \int_{S_j} f_k^j(\vec{\rho}') G^A(\vec{\rho}, \vec{\rho}') d\vec{\rho}' \quad (8)$$

The magnetic flux wrapping the ith ball is expressed as

$$\begin{aligned} \Psi_i &= \sum_{j=1}^N \sum_{k=1}^M a_k^j \psi_k^j(\vec{\rho}) \\ &= \sum_{n=1}^{M \times N} a_n \psi_n(\vec{\rho}) \end{aligned} \quad (9)$$

where

$$a_n = a_k^j$$

$$\psi_n = \psi_k^j$$

$$\forall n : j = \text{floor}\left(\frac{n-1}{M}\right) + 1, k = \text{mod}(n-1, M) + 1$$

Galerkin's method is used to test (9) by the basis functions defined in (2) as

$$\begin{aligned} \langle f_p^i(\vec{\rho}), A(\vec{\rho})h \rangle &= \langle f_m(\vec{\rho}), \Psi(\vec{\rho}) \rangle \\ &= \sum_{n=1}^{M \times N} \left[a_n \langle f_m(\vec{\rho}), \psi_n(\vec{\rho}) \rangle \right] \end{aligned} \quad (10)$$

where

$$f_m(\vec{\rho}) = f_p^i(\vec{\rho}), \forall m : i = \text{floor}\left(\frac{m-1}{M}\right) + 1, p = \text{mod}(m-1, M) + 1$$

Let's define

$$\tilde{\Psi}_m = \tilde{\Psi}_p^i = \langle f_m(\vec{\rho}), \Psi(\vec{\rho}) \rangle \quad (11)$$

$$\tilde{L}_{mn} = \langle f_m(\vec{\rho}), \psi_n(\vec{\rho}) \rangle \quad (12)$$

Substituting (11)(12) into (10) the global weick form equation is obtained as

$$\tilde{\Psi}_m = \sum_{n=1}^{M \times N} [a_n \tilde{L}_{mn}], m=1,2,\dots,M \times N \quad (13)$$

The system matrix is expressed as

$$[\tilde{\Psi}] = [\tilde{L}] \cdot [a] \quad (14)$$

$$\underbrace{\begin{bmatrix} \tilde{\Psi}_1 \\ \tilde{\Psi}_2 \\ \vdots \\ \tilde{\Psi}_{M \times N} \end{bmatrix}}_{\text{modal flux vector}} = \underbrace{\begin{bmatrix} \tilde{L}_{11} & \tilde{L}_{12} & \cdots & \tilde{L}_{1,(M \times N)} \\ \tilde{L}_{21} & \tilde{L}_{22} & \cdots & \tilde{L}_{2,(M \times N)} \\ \vdots & \vdots & \ddots & \vdots \\ \tilde{L}_{(M \times N),1} & \tilde{L}_{(M \times N),2} & \cdots & \tilde{L}_{(M \times N),(M \times N)} \end{bmatrix}}_{\text{modal inductance matrix}} \cdot \underbrace{\begin{bmatrix} a_1 \\ a_2 \\ \vdots \\ a_{M \times N} \end{bmatrix}}_{\text{modal current vector}} \quad (15)$$

Since the BGA balls are small it is reasonable to assume the magnetic potential $A(\vec{\rho})$ to be constant on each conductor. Only zero-order mode contributes to the magnetic potential as

$$\tilde{\Psi}_m = \begin{cases} 2\pi r_i \Psi_i, & \text{if } \text{mod}(m-1, M) = 0 \\ 0, & \text{elsewhere} \end{cases} \quad (17)$$

where Ψ_i is the total flux wrapping the i th "ball".

The modal current in system matrix (14) can be obtained as

$$\begin{aligned} [a] &= [\tilde{L}]^{-1} [\tilde{\Psi}] \\ &= [\tilde{B}] [\tilde{\Psi}] \end{aligned} \quad (18)$$

where $[\tilde{B}] = [\tilde{L}]^{-1}$

The total current on the j th conductor surface is calculated from definition. Since the integral of current density of higher order mode on the conductor is zero, the total current is only related to its zero-order mode by

$$I_j = \int_{S_j} \sum_{k=1}^M a_k^j f_k^j(\vec{\rho}') d\vec{\rho}' = 2\pi r_j a_1^j \quad (19)$$

where the r_j is the radius of the j th conductor.

Substituting (17)(18) into (19) results in

$$I_j = (2\pi)^2 \sum_{i=1}^N \Psi_i \left\{ r_i r_j [\tilde{B}_{mn}]_{(i-1)M+1, (j-1)M+1} \right\} \quad (20)$$

$$\Psi_i = \frac{\sum_{j=1}^N I_j [L'_{ij}]}{(2\pi)^2 r_i r_j} \quad (21)$$

where $[L'_{ij}] = \text{inv} \left\{ [\tilde{B}_{mn}]_{(i-1)M+1, (j-1)M+1} \right\}$

Based on the relationship of magnetic flux and current, the partial inductance is obtained as

$$L_{\text{partial},ij} = \frac{\Psi_i}{I_j} = \frac{[L'_{ij}]}{(2\pi)^2 r_i r_j} \quad (22)$$

2.1.3. Evaluation of Partial Inductance Element and System Matrix. The term defined in (8) and (9) can be analytically calculated in (23).

$$\psi_n = \psi_k^j = \begin{cases} -r_j \mu \ln(\rho), k=1 \\ \frac{\mu (r_j)^{\frac{k}{2}+1} \cos\left(\frac{k\theta}{2}\right)}{k(\rho)^{\frac{k}{2}}}, k>1 \text{ and even} \\ \frac{\mu (r_j)^{\frac{k-1}{2}+1} \sin\left(\frac{(k-1)\theta}{2}\right)}{(k-1)(\rho)^{\frac{k-1}{2}}}, k>1 \text{ and odd} \end{cases} \quad (23)$$

where $\forall n: j = \text{floor}\left(\frac{n-1}{M}\right) + 1, k = \text{mod}(n-1, M) + 1$, ρ and θ are in the local coordinate centered at the j th BGA.

The modal inductance element defined in (12) is obtained from the inner product. When the basis function in the source and the testing basis function are in the same local coordinate, as shown in Figure 2.3, the inner product of different order of basis functions is zero due to the orthogonal of basis functions. And the analytical expressions are obtained as

$$\tilde{L}_{mn} = \begin{cases} -2\pi\mu r_j^2 \ln(r_j), k = p = 1 \\ \frac{r_j^2 \pi\mu}{2\left(\frac{k}{2}\right)}, k = p = 2, 4, \dots, N \\ \frac{r_j^2 \pi\mu}{2\left(\frac{k-1}{2}\right)}, k = p = 3, 5, \dots, N \\ 0, \text{elsewhere} \end{cases} \quad (24)$$

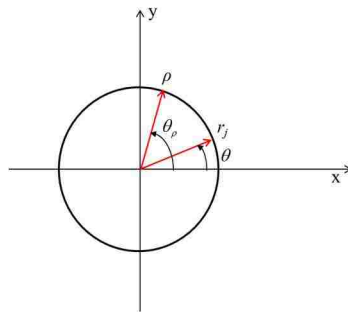


Figure 2.3. Two basis functions are in the same local coordinate

When the testing basis function and the basis function in source are in two different local coordinate systems as shown in Figure 2.4, the location of basis function in source current density needs to be converted to local coordinate of testing basis function. And the inner product is calculated by 1D Gaussian quadrature [72].

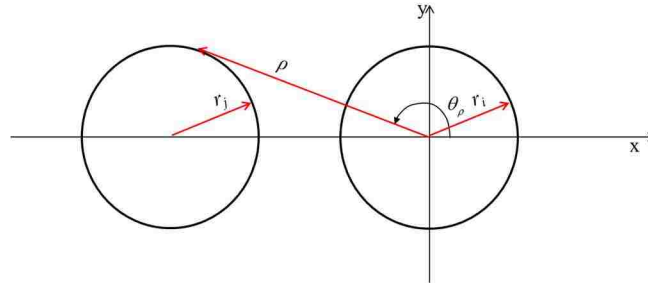


Figure 2.4. Two basis functions are in the different local coordinate

2.1.4. Equivalent Loop Inductance for Signal and Ground Balls. The partial inductance matrix is obtained in (20). A matrix reduction approach is proposed to extract the physical loop inductance. The voltage and current for BGA ball structure are illustrated in Figure 2.5. I_1 to I_M are current flowing through signal balls. I_{M+1} to I_{M+N} are current flowing through ground balls. Voltage is similarly defined for signal balls and ground balls.

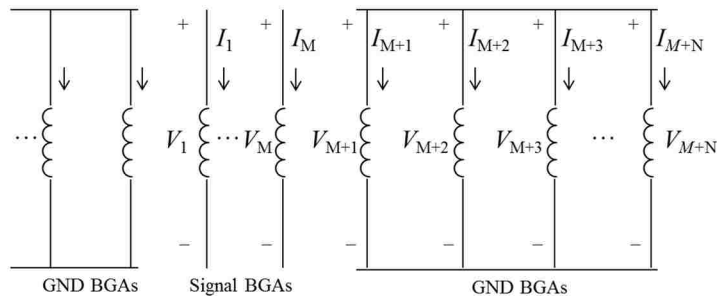


Figure 2.5. The illustration of voltage and current for BGA balls.

The relationship between voltage and current of each conductor is formed by KVL as

$$\begin{bmatrix} V_1 \\ \vdots \\ V_M \\ V_{M+1} \\ \vdots \\ V_{M+N} \end{bmatrix} = j\omega [L_{partial}] \begin{bmatrix} I_1 \\ \vdots \\ I_M \\ I_{M+1} \\ \vdots \\ I_{M+N} \end{bmatrix} \quad (25)$$

where $[L_{partial}]$ is the partial inductance matrix from (22).

M and N are the number of signal BGA balls and ground BGA balls, respectively. The KVL matrix is converted to (26).

$$\begin{bmatrix} I_1 \\ \vdots \\ I_M \\ I_{M+1} \\ \vdots \\ I_{M+N} \end{bmatrix} = \frac{1}{j\omega} [\Gamma_{partial}] \begin{bmatrix} V_1 \\ \vdots \\ V_M \\ V_{M+1} \\ \vdots \\ V_{M+N} \end{bmatrix} \quad (26)$$

where $[\Gamma_{partial}] = [L_{partial}]^{-1}$.

In the pin map, the signal BGA balls and ground BGA balls are close to each other so that current flowing through signal balls returns back through ground balls as

$$-(I_1 + \dots + I_M) = I_{M+1} + I_{M+2} + \dots + I_{M+N} \quad (27)$$

Since the ground BGA balls surrounding the signal BGA balls are next to each other in local region, the potential of all local BGA balls are the same as

$$V_{M+1} = V_{M+2} = \dots = V_{M+N} = V_G \quad (28)$$

By these two conditions the KVL matrix in (26) are simplified as

$$\begin{bmatrix} I_1 \\ \vdots \\ I_M \\ -\sum_{k=1}^M I_k \end{bmatrix} = \frac{1}{j\omega} \begin{bmatrix} \Gamma_{partial 11} & \cdots & \Gamma_{partial 1M} & \sum_{m=M+1}^{M+N} \Gamma_{partial 1m} \\ \vdots & \ddots & \vdots & \vdots \\ \Gamma_{partial M1} & \cdots & \Gamma_{partial MM} & \sum_{m=M+1}^{M+N} \Gamma_{partial Mm} \\ \sum_{n=M+1}^{M+N} \Gamma_{partial n1} & \cdots & \sum_{n=M+1}^{M+N} \Gamma_{partial nM} & \sum_{n=M+1}^{M+N} \sum_{m=M+1}^{M+N} \Gamma_{partial nm} \end{bmatrix} \begin{bmatrix} V_1 \\ \vdots \\ V_M \\ V_G \end{bmatrix} \quad (29)$$

The matrix in (28) is converted to

$$\begin{bmatrix} V_1 \\ \vdots \\ V_M \\ V_G \end{bmatrix} = j\omega \begin{bmatrix} L'_{partial 1,1} & \cdots & L'_{partial 1M} & L'_{partial 1,M+1} \\ \vdots & \ddots & \vdots & \vdots \\ L'_{partial M,1} & \cdots & L'_{partial M,M} & L'_{partial M,M+1} \\ L'_{partial M+1,1} & \cdots & L'_{partial M+1,M} & L'_{partial M+1,M+1} \end{bmatrix} \begin{bmatrix} I_1 \\ \vdots \\ I_M \\ -\sum_{k=1}^M I_k \end{bmatrix} \quad (30)$$

where

$$[L'_{partial}] = \begin{bmatrix} \Gamma_{partial 11} & \cdots & \Gamma_{partial 1M} & \sum_{m=M+1}^{M+N} \Gamma_{partial 1m} \\ \vdots & \ddots & \vdots & \vdots \\ \Gamma_{partial M1} & \cdots & \Gamma_{partial MM} & \sum_{m=M+1}^{M+N} \Gamma_{partial Mm} \\ \sum_{n=M+1}^{M+N} \Gamma_{partial n1} & \cdots & \sum_{n=M+1}^{M+N} \Gamma_{partial nM} & \sum_{n=M+1}^{M+N} \sum_{m=M+1}^{M+N} \Gamma_{partial nm} \end{bmatrix}^{-1}$$

The current flowing through signal BGA ball and back from the surrounding ground BGA balls forms a loop. The physical loop inductance is calculated as

$$\begin{aligned} L_{loop ij} &= \frac{V_i - V_G}{j\omega I_j} \\ &= (L'_{partial i,j} - L'_{partial M+1,j}) - (L'_{partial i,M+1} - L'_{partial M+1,M+1}) \end{aligned} \quad (31)$$

2.1.5. Equivalent Loop Inductance for Power and Ground Balls. Equivalent inductance is important factor in power integrity. The smaller the equivalent inductance seen from IC, the less voltage fluctuation in the power net. The illustration figure for power and ground net is shown as

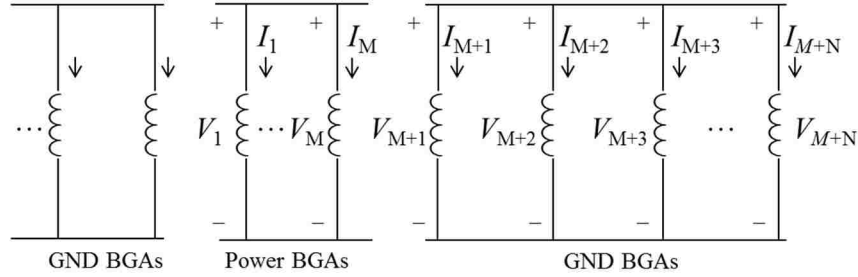


Figure 2.6. Illustration figure for power and ground net

The current flowing through power balls returns back through the ground balls as

$$I = I_1 + \dots + I_M = -(I_{M+1} + I_{M+2} + \dots + I_{M+N}) \quad (32)$$

Voltage on the local power balls are the same and voltage on the local ground balls are the same as

$$V_1 = V_2 = \dots = V_M = V_P \quad (33)$$

$$V_{M+1} = V_{M+2} = \dots = V_{M+N} = V_G \quad (34)$$

Similar to the expression from (25) to (31), the relationship between voltage and current is established as

$$\begin{bmatrix} I \\ -I \end{bmatrix} = \frac{1}{j\omega} \begin{bmatrix} \sum_{n=1}^N \sum_{m=1}^N \Gamma_{\text{partial } nm} & \sum_{n=1}^N \sum_{m=M+1}^{M+N} \Gamma_{\text{partial } nm} \\ \sum_{n=M+1}^{M+N} \sum_{m=1}^N \Gamma_{\text{partial } nm} & \sum_{n=M+1}^{M+N} \sum_{m=M+1}^{M+N} \Gamma_{\text{partial } nm} \end{bmatrix} \begin{bmatrix} V_P \\ V_G \end{bmatrix} \quad (35)$$

The equation (35) is converted to

$$\begin{bmatrix} V_P \\ V_G \end{bmatrix} = j\omega \begin{bmatrix} L'_{partial\ 1,1} & L'_{partial\ 1,2} \\ L'_{partial\ 2,1} & L'_{partial\ 2,2} \end{bmatrix} \begin{bmatrix} I \\ -I \end{bmatrix} \quad (36)$$

where $[L'] = [\Gamma]^{-1}$.

The loop inductance is obtained as

$$L_{loop} = \frac{V_P - V_G}{j\omega I} = L'_{partial\ 1,1} - L'_{partial\ 1,2} + L'_{partial\ 2,1} + L'_{partial\ 2,2} \quad (37)$$

2.2. EQUIVALENT CAPACITANCE CALCULATION

The cross section of BGA ball structure is separated into two portions: coaxial anti-pad aperture region and BGA ball-plate region as [8] in Figure 2.7.

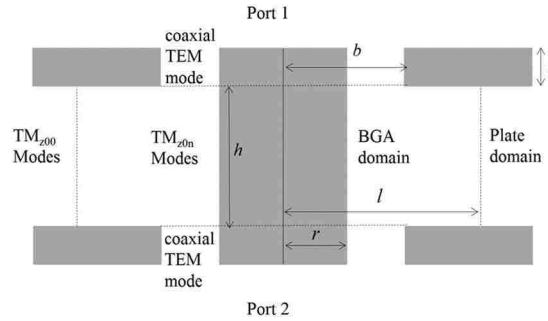


Figure 2.7. Segmentation of BGA balls and a parallel plate pair

In the anti-pad aperture the coaxial capacitance is

$$C_a = \frac{2\pi\epsilon_r\epsilon_0 t}{\ln\left(\frac{b}{r}\right)} \quad (38)$$

where r and b are radius of the BGA ball and anti-pad, respectively. t is the plane thickness.

In the BGA ball-plate region, the capacitance between conductor and parallel plates is derived in [1] as

$$C_h = \frac{j4\varepsilon\pi^2 r}{h \ln(b/r)} \sum_{n=1,3,4,\dots}^{2N-1} F_n^S(r) \quad (39)$$

where h is the distance between two parallel plate. The auxiliary function $F_n^S(r)$ is

$$\begin{aligned} F_n^S(\rho) &= \frac{(1 - \Gamma_r^{(n)} \Gamma_l^{(n)})^{-1}}{k_n (1 + \delta_{n0})} \\ &\cdot \left\{ \left[H_0^{(2)}(k_n b) - H_0^{(2)}(k_n r) \right] + \Gamma_l^{(n)} \left[J_0(k_n b) - J_0(k_n r) \right] \right\} \\ &\cdot \left[J_1(k_n \rho) + \Gamma_r^{(n)} H_1^{(2)}(k_n \rho) \right] \end{aligned} \quad (40)$$

where $\Gamma_r^{(n)}$ and $\Gamma_l^{(n)}$ are the reflection coefficients for the n th cylindrical waves from the BGA ball and the outer boundary.

$$\Gamma_r^{(n)} = -\frac{J_0(k_n r)}{H_0^{(2)}(k_n r)} \quad (41)$$

$$\Gamma_l^{(n)} = \begin{cases} -\frac{H_0^{(2)}(k_n l)}{J_0(k_n l)} & \text{PEC} \\ -\frac{H_1^{(2)}(k_n l)}{J_1(k_n l)} & \text{PMC} \\ 0 & \text{PML} \end{cases} \quad (42)$$

where $J_{0(1)}(k_n r)$ and $H_{0(1)}^{(2)}(k_n r)$ are the zeroth (first) order Bessel and Hankel functions of the second kind, respectively. kn is the wavenumber.

$$k_n = \sqrt{k_0^2 \varepsilon_r - \left(\frac{n\pi}{h} \right)^2} \quad (43)$$

The capacitance of BGA ball to ground plane is obtained as

$$C_{BGA} = C_a + C_h \quad (44)$$

2.3. EQUIVALENT CIRCUIT FOR SIGNAL AND GROUND BALLS

Since BGA balls are electrically small in the frequency range of interest, lumped inductance and capacitance are developed to represent for the BGA balls. The loop inductance and capacitance are obtained from (31)(44), respectively. An equivalent circuit in π topology is established with lumped L and C, as shown in Figure 2.8. L11 and L22 are self-inductance. L12 is the mutual inductance. CBGA is the capacitance from BGA ball to top or bottom plates.

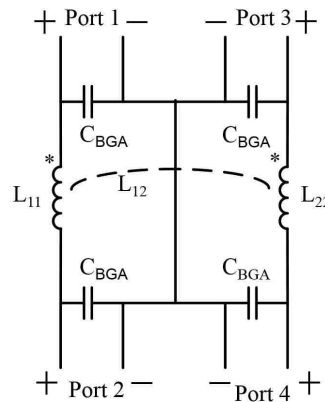


Figure 2.8. The equivalent circuit model for BGA balls

The structure with BGA balls and parallel plates is modeled in full-wave simulator HFSS, Ansys, as shown in Figure 2.9. BGA pitch size is 1mm. BGA diameter is 0.6637mm. BGA height is 0.337mm. The anti-pad diameter is 0.77mm. Two signal BGA balls are asymmetrically surrounded by eleven ground BGA balls. Four ports are set up at the anti-pad region in the two ground planes.

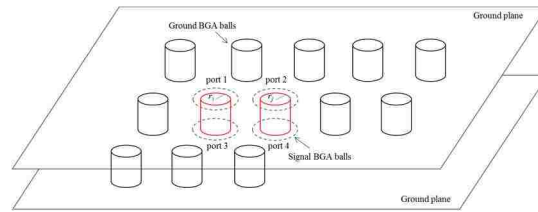


Figure 2.9. BGA ball structures in full-wave simulator

The capacitance of the BGA ball to ground plane pairs is obtained by (42) with PML boundary as 35.2 fF.

The inductance are calculated by (29) and are compared with full-wave simulation in Table 2.1. They have good agreement in both self and mutual inductance. It takes less than 5 seconds for the calculation.

Table 2.1. Inductance validation between analytical method and full-wave simulation

	Self-inductance	Mutual Inductance
Full-wave simulation	62 pH	13.3 pH
Analytical calculation (10 order modes)	61 pH	13.6 pH
Analytical calculation (zero order modes)	75.1 pH	20.8 pH

When inductance and capacitance are obtained, the equivalent circuit is built. The equivalent circuit is simulated from DC to 40 GHz using the Advanced Design System (ADS), a circuit simulator from Keysight. The S-parameters of differential mode and common mode are compared between equivalent circuit and full-wave simulation in both

magnitude and phase as shown in Figure 2.10 and Figure 2.11. The differences in insertion loss and return loss from differential mode are only 0.03 dB and 0.34dB at 40 GHz, respectively. The differences for common mode insertion loss and return loss are only 0.04 dB and 0.13dB at 40 GHz, respectively.

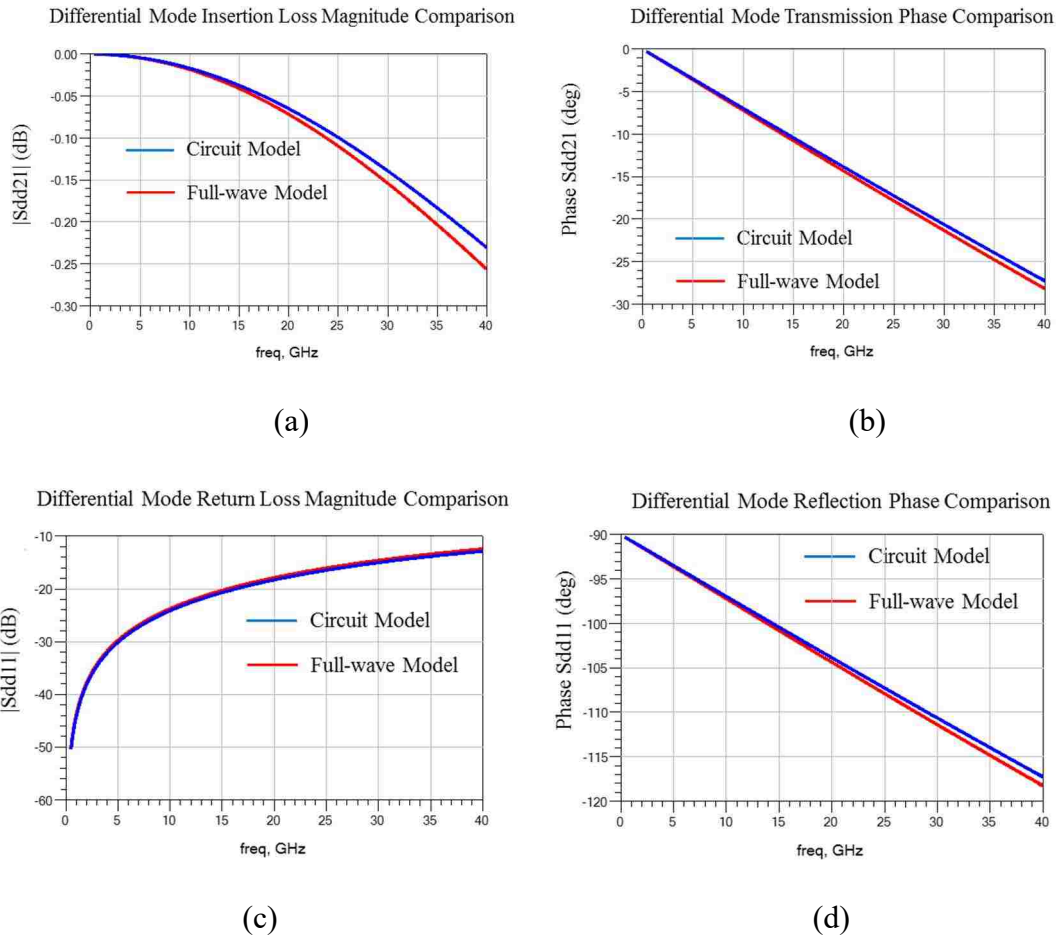


Figure 2.10. Comparison of differential mode S-parameters. (a) insertion loss comparison in magnitude (b) insertion loss comparison in phase (c) return loss comparison in magnitude (d) return loss comparison in phase

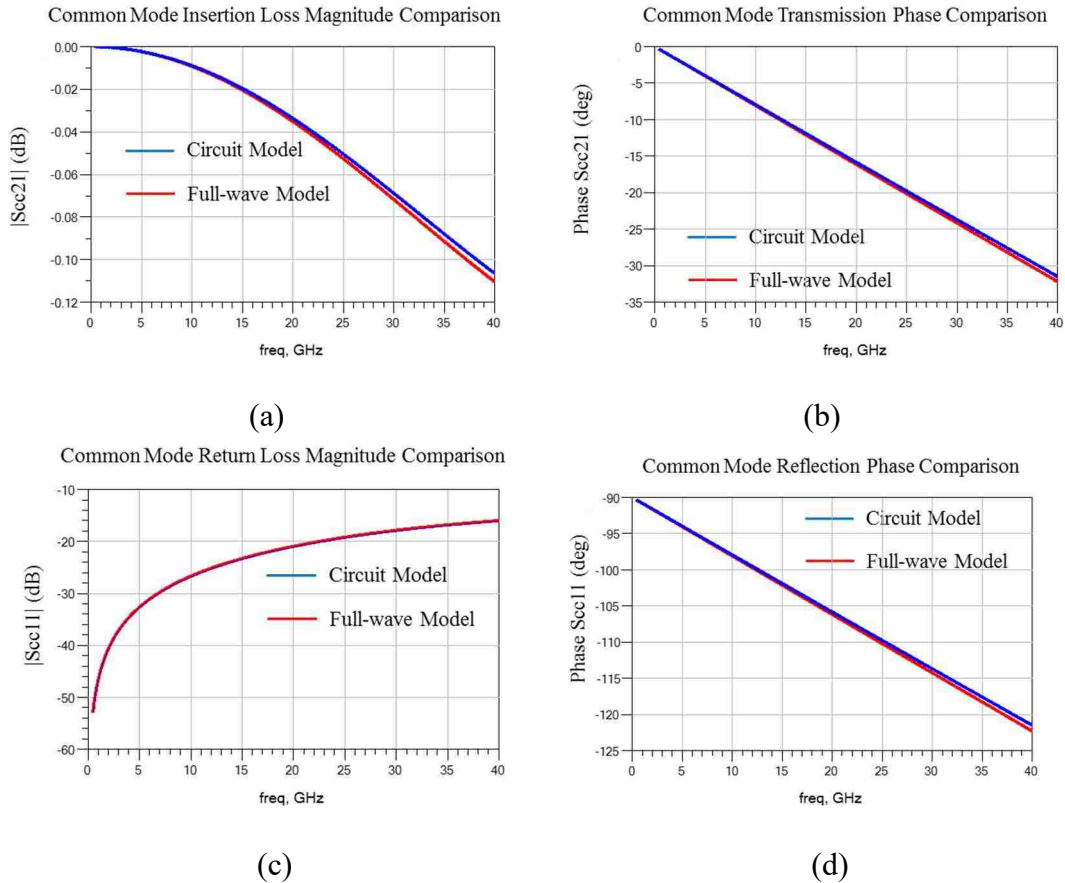


Figure 2.11. Comparison of common mode S-parameters. (a) insertion loss comparison in magnitude (b) insertion loss comparison in phase (c) return loss comparison in magnitude (d) return loss comparison in phase

2.4. GUIDELINE FOR POWER GROUND BALL PATTERN

Since there are variant configurations for power and ground solder ball pin maps, it is necessary to select the pin map which has less equivalent inductance. In the proposed method, the equivalent inductance can be accurately and efficiently obtained and provide the guideline for the pin map optimization.

There are two patterns shown as Figure 2.12. BGA pitch size is 1mm. BGA diameter is 0.6637mm. BGA height is 0.337mm. Comparing the equivalent inductance from two different patterns in Table 2.2 and Table 2.3, there is less inductance in the alternate pin pattern and is good be used to maintain power integrity.

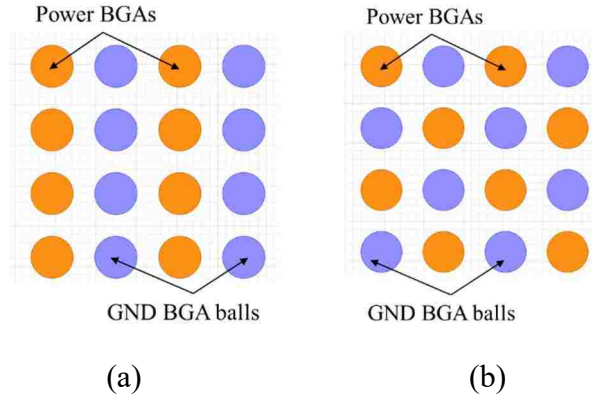


Figure 2.12. Different power ground ball patterns. (a) column pattern (b) alternate pattern

Table 2.2. Equivalent inductance from column pattern

BGA diameter	FEM	Analytical Solution
20.72 mil	21.3pH	21.2pH
24 mil	17.9pH	17.8pH
26.13 mil	15.8pH	15.7pH

Table 2.3. Equivalent inductance from alternate pattern

BGA diameter	FEM	Analytical Solution
20.72 mil	13.6pH	13.5pH
24 mil	11.1pH	11.0pH
26.13 mil	9.5pH	9.4pH

Physical capacitance and inductance are calculated with analytical solution and fast modal-based method, respectively. The effect of the non-uniformly distributed current in BGA structures is carefully considered in the proposed approach. Image theory is also used to convert 3D problem to the 2D problem to reduce the computation complex order. A generic spice model is built and is validated with full-wave simulations. Good correlation between full-wave simulation and generic circuit model can be achieved up to 40GHz in both magnitude and phase. The generic circuit model can be used for the

product design in pre-layout stage and it can accurately predict the channel behavior in a few seconds and provides a fast way to optimize the design. The equivalent inductance for different power and ground pin maps can be accurately and efficiently calculated. It can be used to determine the power and ground ball patterns for less power noise in the digital circuit system.

3. MODAL BASED INDUCTANCE EXTRACTION

Power distributed network (PDN) is one of the foundations in the high-speed digital system. The power distributed network of the printed circuit board is to provide power supply to the functioning ICs. When the transistors turn on and off there is switching current draw from the power network. A large voltage fluctuation could be induced and the ICs may malfunction. The voltage ripple can propagate on the power network which couples to the transmission line or via structures and cause SI issues [73] or interfaces with other ICs and cause RFI issues. When the voltage ripple approaches to the edge of the power distributed network it will radiated out of the printed circuit board and cause EMI issues [48][49]. The objective of power distributed network design is to minimize the voltage fluctuation to be within the requirement for normal functioning [74].

There are several methodologies to calculate the power distributed network impedance (Z_{pp}). Numerical methods including finite difference time domain method (FDTD) and finite element method (FEM) are introduced in [75]. Full-wave simulations can be used to model parallel plate with BGAs and statistical methods can be used to estimate crosstalk [64]. The circuit model for power distributed network can be extracted from transmission line method, partial element equivalent circuit method [53]. The resonant cavity formulation based methodologies are also introduced in [76][77]. The equivalent inductance seen from ICs is an important factor. The less the equivalent inductance the less the voltage ripple on the power distributed network will be induced. The inductance extraction approaches are introduced in [78]-[81]. These methodologies provide solutions to model power distributed network. The assumptions in these methods are the current is uniformly distributed around the conductor. However, structure for the parallel plates with BGAs in between is a different story. Since the solder balls in package are closely placed to each other, the current density is no longer uniformly distributed. Current density will be crowding and this proximity effect affects the efficiency and performance of the power distributed network. The lack of consideration of proximity effect will introduce errors in the estimation of power noise and also introduce errors in some physics-based via modeling which is also based on the accuracy of parallel plates impedance [7][82][83]. Thus, to accurately estimate the power

distributed network behavior and to minimize the voltage fluctuation the proximity effect has to be carefully considered for the package power network design.

In this paper, the modal-based cavity methodology is proposed. Unlike the traditional resonance cavity method in which the port current distribution is isotropic, the proposed methodology introduces the modal basis functions to accommodate the proximity effect. Modal-based partial inductance is extracted from the modal cavity impedance. And the physical equivalent loop inductance is further obtained. The proposed physics-based equivalent inductance provides the relationship between geometry and the lumped element. Since the modal inductance is from analytical solutions, it is efficiently and accurately to estimate the performance of the target structure. Furthermore, the proposed physics-based methodology does not require mesh during the calculation. Due to the orthogonality property of the modal basis functions the size of the computational matrix is reduced. It reduces the computational time and resources compared with the full-wave methodologies. The proposed methodology demonstrates the effect of boundary to the equivalent inductance and provides the guideline for optimization of the power and ground ball patterns in the PDN design.

3.1. METHODOLOGY OF EQUIVALENT INDUCTANCE CALCULATION

The parallel plates with ball grid arrays (BGAs) placed in between is shown in Figure 3.1. The balls are approximated as cylinders instead of spheres. The current flowing through BGA balls is perpendicular to the two parallel plates. When the distance between two parallel plates is electrically small there is no variation along axial direction. The two parallel plates structure is treated as a 2D resonance cavity structure.

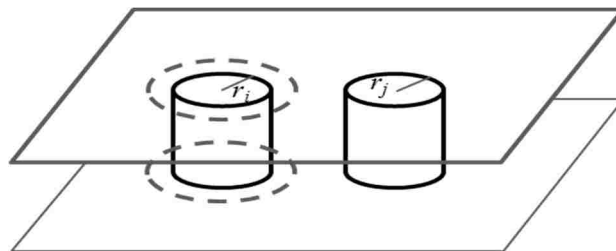


Figure 3.1. Parallel plate structure with BGA balls

3.1.1. Basis Functions. Since the BGAs are placed close to each other, the distance between adjacent BGAs is comparable to the BGA diameter. The current density of the BGAs are not uniformly distributed. When modeling two parallel plates with BGAs the proximity effect needs to be carefully considered. It is reasonable to assume that the BGA balls are perfect electric conductor so all the current flows along the edge of the BGA balls. Similar to Fourier Series, the current density is expanded by two orthogonal basis functions and is expressed as a summation of modal current densities as

$$J^j(\vec{\rho}') = \sum_{k=1}^M a_k^j f_k^j(\vec{\rho}') \quad (1)$$

where a_k^j is the unknown modal current density and $f_k^j(\vec{\rho}')$ is the basis function.

$$f_k^j = \begin{cases} 1, & k=1 \text{ (zero order mode)} \\ \cos\left(\frac{k}{2}\theta_j\right), & k > 1 \text{ \& even (higher order mode)} \\ \sin\left(\frac{k-1}{2}\theta_j\right), & k > 1 \text{ \& odd (higher order mode)} \end{cases} \quad (2)$$

where j, k are the index of the conductor and basis function, respectively. M is the total number of basis function. The angle θ_j is defined in local coordinate centered at conductor j.

The zero order basis function denotes as the uniformly distributed current along the conductor. The higher order basis functions represent for the proximity effect of the non-uniformly distributed current distribution along the angular direction[72].

3.1.2. Modal-based Partial Inductance from Cavity Method. The rectangular cavity with PMC boundary surrounding the four sides is introduced in [76]. The E field is expressed as the integral of the Green's function with current density as

$$E_z(\vec{\rho}) = \sum_{j=1}^N \int_{c'} G(\vec{\rho}, \vec{\rho}') J^j(\vec{\rho}') d\vec{\rho}' \quad (3)$$

where $G(r, r')$ is the Green's function in 2D Helmholtz equation for rectangular cavity with four side walls to be the PMC boundary, as

$$G(x, y; x', y') = \frac{j\omega\mu}{ab} \sum_{m=0}^{\infty} \sum_{n=0}^{\infty} \frac{c_m^2 c_n^2}{k_{xm}^2 + k_{yn}^2 - k^2} \cdot \cos(k_{xm}x) \cos(k_{yn}y) \cos(k_{xm}x') \cos(k_{yn}y') \quad (4)$$

where

$$c_m = \begin{cases} 1 & m = 0 \\ \sqrt{2} & m = 1, 2, 3, \dots \end{cases}, c_n = \begin{cases} 1 & n = 0 \\ \sqrt{2} & n = 1, 2, 3, \dots \end{cases}, k_{xm} = \frac{m\pi}{a} \text{ and } k_{yn} = \frac{n\pi}{b}$$

ω is the angular frequency. μ is the permeability. d is the distance between two parallel plates. a and b are rectangular side wall length in x and y direction, respectively. m and n are the m th and n th eigenmode in the x and y direction, respectively.

Since there is no E field variation along the z direction, the voltage between the two parallel plates is expressed as

$$V = E_z \cdot d \quad (5)$$

Substitute (1)(3) into (5) results in the voltage between i th ball as

$$\begin{aligned} V_i(\bar{\rho}) &= \sum_{j=1}^N \sum_{k=1}^M a_k^j d \int_{c'} G(\bar{\rho}, \bar{\rho}') f_k^j(\bar{\rho}') d\bar{\rho}' \\ &= \sum_{n=1}^{M \times N} a_n d \int_{c'} G(\bar{\rho}, \bar{\rho}') f_n(\bar{\rho}') d\bar{\rho}' \end{aligned} \quad (6)$$

where

$$a_n = a_k^j, f_n = f_k^j$$

$$\forall n: j = \text{floor}\left(\frac{n-1}{M}\right) + 1, k = \text{mod}(n-1, M) + 1$$

Galerkin's method is used to test (6) by the basis functions defined in (2) as

$$\begin{aligned}
\langle f_p^i(\bar{\rho}), V_i(\bar{\rho}) \rangle &= \langle f_m(\bar{\rho}), V_i(\bar{\rho}) \rangle \\
&= \sum_{n=1}^{M \times N} \left[a_n \langle f_m(\bar{\rho}), d \int_{c'} G(\bar{\rho}, \bar{\rho}') f_n(\bar{\rho}') d\bar{\rho}' \rangle \right] \\
&= \sum_{n=1}^{M \times N} \left[a_n \cdot d \int_{c'} \int_{c'} G(\bar{\rho}, \bar{\rho}') f_m(\bar{\rho}) f_n(\bar{\rho}') d\bar{\rho}' d\bar{\rho} \right]
\end{aligned} \tag{7}$$

where

$$\begin{aligned}
f_m(\bar{\rho}) &= f_p^i(\bar{\rho}) \\
\forall m : i &= \text{floor}\left(\frac{m-1}{M}\right) + 1, p = \text{mod}(m-1, M) + 1
\end{aligned}$$

Let's define

$$\tilde{V}_m = \langle f_m(\bar{\rho}), V_i(\bar{\rho}) \rangle \tag{8}$$

$$\tilde{Z}_{mn} = d \int_{c'} \int_{c'} G(\bar{\rho}, \bar{\rho}') f_m(\bar{\rho}) f_n(\bar{\rho}') d\bar{\rho}' d\bar{\rho} \tag{9}$$

The equation (9) can be explicitly expressed as

$$\begin{aligned}
\tilde{Z}_{mn} &= \frac{j\omega\mu d}{ab} \sum_{m=0}^{\infty} \sum_{n=0}^{\infty} \frac{c_m^2 c_n^2}{k_{xm}^2 + k_{yn}^2 - k^2} \\
&\cdot \int_0^{2\pi} \cos[k_{xm}(X_i + r_i \cos \theta)] \cos[k_{yn}(Y_i + r_i \sin \theta)] f_m(\bar{\rho}) r_i d\theta \\
&\cdot \int_0^{2\pi} \cos[k_{xm}(X_j + r_j \cos \theta')] \cos[k_{yn}(Y_j + r_j \sin \theta')] f_n(\bar{\rho}') r_j d\theta'
\end{aligned} \tag{10}$$

where (X_j, Y_j) and (X_i, Y_i) are the centers of the source conductor and the observation conductor in global coordinate, respectively. θ and θ' are the angles in the local polar coordinates of the observation and source, as shown in Figure 3.2.

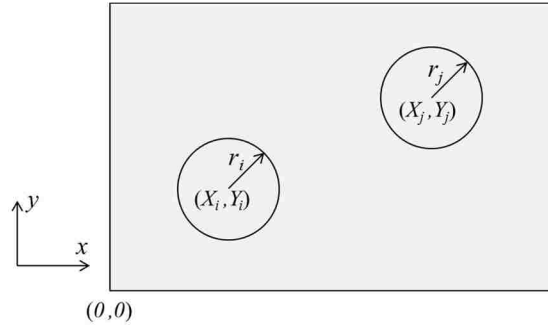


Figure 3.2. Rectangular cavity structure with circular ports

The inductance extraction approach [101] is used to obtain the modal inductance from the impedance in (10) as

$$\begin{aligned}
 \tilde{L}_{mn} &= \frac{\mu d}{ab} \sum_{m=0}^{\infty} \sum_{n=0}^{\infty} \frac{c_m^2 c_n^2}{k_{xm}^2 + k_{yn}^2} \\
 &\cdot \int_0^{2\pi} \cos[k_{xm}(X_i + r_i \cos \theta)] \cos[k_{yn}(Y_i + r_i \sin \theta)] f_m(\bar{\rho}) r_i d\theta \\
 &\cdot \int_0^{2\pi} \cos[k_{xm}(X_j + r_j \cos \theta')] \cos[k_{yn}(Y_j + r_j \sin \theta')] f_n(\bar{\rho}') r_j d\theta' \\
 &= \sum_{m=0}^{\infty} \sum_{n=0}^{\infty} K \cdot T_i T_j
 \end{aligned} \tag{11}$$

where

$$K = \frac{\mu d}{ab} \frac{c_m^2 c_n^2}{k_{xm}^2 + k_{yn}^2}$$

$$T_i = \int_0^{2\pi} \cos[k_{xm}(X_i + r_i \cos \theta)] \cdot \cos[k_{yn}(Y_i + r_i \sin \theta)] f_m(\bar{\rho}) r_i d\theta$$

$$T_j = \int_0^{2\pi} \cos[k_{xm}(X_j + r_j \cos \theta)] \cdot \cos[k_{yn}(Y_j + r_j \sin \theta)] f_n(\bar{\rho}) r_j d\theta$$

Substituting (8)(11) into (7) the global weak form equation is obtained as

$$\tilde{V}_m = \sum_{n=1}^{M \times N} [a_n \tilde{L}_{mn}], m = 1, 2, \dots, M \times N \tag{12}$$

where \tilde{V}_m is modal voltage, \tilde{L}_{mn} is modal inductance, a_n is the modal current.

The system matrix is expressed as

$$[\tilde{V}] = [\tilde{L}] \cdot [a] \quad (13)$$

where $[\tilde{V}]$ is modal voltage vector, $[\tilde{L}]$ is modal inductance matrix, $[a]$ is the modal current vector.

The voltage $V(\vec{\rho})$ is constant on each conductor. So only the zero-order mode contributes to the modal voltage $[\tilde{V}]$ as

$$\tilde{V}_m = \begin{cases} 2\pi r_i V_i, & \text{if } \text{mod}(m-1, M) = 0 \\ 0, & \text{elsewhere} \end{cases} \quad (14)$$

where V_i is the voltage between the i th ball.

The modal current vector in system matrix (13) is obtained as

$$\begin{aligned} [a] &= [\tilde{L}]^{-1} [\tilde{\Psi}] \\ &= [\tilde{B}] [\tilde{\Psi}] \end{aligned} \quad (15)$$

where $[\tilde{B}] = [\tilde{L}]^{-1}$.

The total current along the j th conductor surface is obtained from the definition as

$$I_j = \int_{S_j} \sum_{k=1}^M a_k^j f_k^j(\vec{\rho}') d\vec{\rho}' = 2\pi r_j a_1^j \quad (16)$$

where the r_j is the radius of the j th conductor

Since the integral of current density of higher order mode on the conductor is zero, the total current is only related to its zero-order mode.

Substitute (14)(15) into (16) results in

$$I_j = (2\pi)^2 \sum_{i=1}^N V_i \left\{ r_i r_j [\tilde{B}_{mn}]_{(i-1)M+1, (j-1)M+1} \right\} \quad (17)$$

The voltage is obtained as

$$V_i = \frac{\sum_{j=1}^N I_j [L'_{ij}]}{(2\pi)^2 r_i r_j} \quad (18)$$

where $[L'_{ij}] = \left([\tilde{B}_{mn}]_{(i-1)M+1, (j-1)M+1} \right)^{-1}$

Based on the ohm's law, the partial inductance is obtained as

$$L_{partial,ij} = \frac{V_i}{I_j} = \frac{[L'_{ij}]}{(2\pi)^2 r_i r_j} \quad (19)$$

3.1.3. System Matrix Calculation. The two integrals, T_i and T_j , in (11) are in the same form and can be similarly solved. The first integral in (11) T_i is decomposed as

$$T_i = P_{i1} + P_{i2} + P_{i3} + P_{i4} \quad (20)$$

where

$$\begin{aligned} P_{i1} &= \cos(k_{xm} X_i) \cos(k_{yn} Y_i) \\ &\cdot \int_0^{2\pi} \cos(k_{xm} r_i \cos \theta) \cos(k_{yn} r_i \sin \theta) f_m(\bar{\rho}) r_i d\theta \\ P_{i2} &= \sin(k_{xm} X_i) \sin(k_{yn} Y_i) \\ &\cdot \int_0^{2\pi} \sin(k_{xm} r_i \cos \theta) \sin(k_{yn} r_i \sin \theta) f_m(\bar{\rho}) r_i d\theta \\ P_{i3} &= -\cos(k_{xm} X_i) \sin(k_{yn} Y_i) \\ &\cdot \int_0^{2\pi} \cos(k_{xm} r_i \cos \theta) \sin(k_{yn} r_i \sin \theta) f_m(\bar{\rho}) r_i d\theta \\ P_{i4} &= -\sin(k_{xm} X_i) \cos(k_{yn} Y_i) \\ &\cdot \int_0^{2\pi} \sin(k_{xm} r_i \cos \theta) \cos(k_{yn} r_i \sin \theta) f_m(\bar{\rho}) r_i d\theta \end{aligned}$$

The term $\cos(z \cos \theta)$, $\cos(z \sin \theta)$, $\sin(z \cos \theta)$ and $\sin(z \sin \theta)$ in $P_{i1} \sim P_{i4}$ can be analytically expanded by Generating function [85].

When the basis function $f_m(\theta)$ is zero order, P_{i1} in (20) is expressed as

$$P_{i1} = \cos(k_{xm} X_i) \cos(k_{yn} Y_i) \cdot \sum_{p=-\infty}^{\infty} \sum_{q=-\infty}^{\infty} \left\{ (-1)^p J_{2p}(k_{xm} r_i) J_{2q}(k_{yn} r_i) \int_0^{2\pi} \cos(2p\theta) \cos(2q\theta) r_i d\theta \right\} \quad (21)$$

P_{i1} is non-zero only when $|2p\theta| = |2q\theta|$ according to the orthogonal property of cos function

$$P_{i1} = 2\pi r_i \cos(k_{xm} X_i) \cos(k_{yn} Y_i) \cdot \left[J_0(k_{xm} r_i) J_0(k_{yn} r_i) + 2 \sum_{p=1}^{\infty} (-1)^p J_{2p}(k_{xm} r_i) J_{2p}(k_{yn} r_i) \right] \quad (22)$$

The addition theorem of Bessel function is introduced as

$$J_0(\sqrt{\alpha^2 + \beta^2}) = J_0(\alpha) J_0(\beta) + 2 \sum_{k=1}^{\infty} (-1)^k J_{2k}(\alpha) J_{2k}(\beta) \quad (23)$$

Applying the addition theorem P_{i1} is obtained and it is the same as in [102]

$$P_{i1} = \cos(k_{xm} X_i) \cos(k_{yn} Y_i) J_0\left(r_i \sqrt{k_{xm}^2 + k_{yn}^2}\right) 2\pi r_i \quad (24)$$

Similarly P_{i2} , P_{i3} , P_{i4} are solved as

$$P_{i2} = P_{i3} = P_{i4} = 0 \quad (25)$$

The integral T_i for zero order basis function is obtained as

$$T_{i,0} = P_{i1} + P_{i2} + P_{i3} + P_{i4} = P_{i1} \quad (26)$$

When the even order basis function $f_m(\theta)$ is involved, P_{i1} in (20) is expressed as

$$\begin{aligned} P_{i1} &= \cos(k_{xm} X_i) \cos(k_{yn} Y_i) \\ &\cdot \sum_{p=-\infty}^{\infty} \sum_{q=-\infty}^{\infty} \left\{ (-1)^p J_{2p}(k_{xm} r_i) J_{2q}(k_{yn} r_i) \right. \\ &\quad \left. \int_0^{2\pi} \cos(2p\theta) \cos(2q\theta) \cos\left(\frac{k}{2}\theta\right) r_i d\theta \right\} \end{aligned} \quad (27)$$

The integral in (27) is

$$\begin{aligned} &\int_0^{2\pi} \cos(2p\theta) \cos(2q\theta) \cos\left(\frac{k}{2}\theta\right) r_i d\theta = \\ &\int_0^{2\pi} \frac{1}{2} \left\{ \cos\left[\left(2p - \frac{k}{2}\right)\theta\right] + \cos\left[\left(2p + \frac{k}{2}\right)\theta\right] \right\} \cos(2q\theta) r_i d\theta \end{aligned} \quad (28)$$

According to the orthogonal property, the P_{i1} is only non-zero when $\frac{k}{2}$ is even and

$$|2q| = \left| 2p - \frac{k}{2} \right| \text{ or } |2q| = \left| 2p + \frac{k}{2} \right|. \text{ With the property of Bessel function } J_{-n}(x) = (-1)^n J_n(x)$$

, P_{i1} in (27) is obtained as

$$\begin{aligned} P_{i1} &= 2\pi r_i \cos(k_{xm} X_i) \cos(k_{yn} Y_i) \\ &\cdot \left\{ J_0(k_{xm} r_i) J_{\frac{k}{2}}(k_{yn} r_i) + \sum_{p=1}^{\infty} (-1)^p J_{2p}(k_{xm} r_i) \left[J_{2p+\frac{k}{2}}(k_{yn} r_i) + J_{2p-\frac{k}{2}}(k_{yn} r_i) \right] \right\} \end{aligned} \quad (29)$$

P_{i4} with even order basis function in (20) is expressed as

$$\begin{aligned}
 P_{i4} &= -\sin(k_{xm}X_i)\cos(k_{yn}Y_i) \\
 &\cdot \sum_{p=-\infty}^{\infty} \sum_{q=-\infty}^{\infty} \left\{ (-1)^p J_{2p+1}(k_{xm}r_i) J_{2q}(k_{yn}r_i) \right. \\
 &\left. \int_0^{2\pi} \frac{1}{2} \left\{ \cos \left[\left(2p+1 - \frac{k}{2} \right) \theta \right] + \cos \left[\left(2p+1 + \frac{k}{2} \right) \theta \right] \right\} \cos(2q\theta) r_i d\theta \right\}
 \end{aligned} \tag{30}$$

According to the orthogonal property, the P_{i4} is only non-zero when $\frac{k}{2}$ is odd and

$$|2q| = \left| 2p+1 - \frac{k}{2} \right| \text{ or } |2q| = \left| 2p+1 + \frac{k}{2} \right|, \text{ leading to}$$

$$\begin{aligned}
 P_{i4} &= -2\pi r_i \sin(k_{xm}X_i) \cos(k_{yn}Y_i) \\
 &\cdot \sum_{p=0}^{\infty} (-1)^p J_{2p+1}(k_{xm}r_i) \left[J_{2p+1-\frac{k}{2}}(k_{yn}r_i) + J_{2p+1+\frac{k}{2}}(k_{yn}r_i) \right]
 \end{aligned} \tag{31}$$

The integral T_i for even order basis function is obtained as

$$T_{i,even} = P_{i1} + P_{i2} + P_{i3} + P_{i4} = \begin{cases} P_{i1}, & \frac{k}{2} \text{ is even} \\ P_{i4}, & \frac{k}{2} \text{ is odd} \end{cases} \tag{32}$$

Similarly, P_{i2} and P_{i3} with even order basis functions are solved as

$$P_{i2} = P_{i3} = 0 \tag{33}$$

When the even order basis function $f_m(\theta)$ is involved, P_{i2} in (20) is expressed as

$$\begin{aligned}
 P_{i2} &= \sin(k_{xm}X_i)\sin(k_{yn}Y_i) \\
 &\cdot \sum_{p=-\infty}^{\infty} \sum_{q=-\infty}^{\infty} \left\{ (-1)^p J_{2p+1}(k_{xm}r_i) J_{2q+1}(k_{yn}r_i) \int_0^{2\pi} \frac{1}{2} \left[\sin \left(\frac{k-1}{2} - 2p-1 \right) \theta + \sin \left(\frac{k-1}{2} + 2p+1 \right) \theta \right] \sin[(2q+1)\theta] r_i d\theta \right\}
 \end{aligned} \tag{34}$$

The P_{i2} is only non-zero when $\frac{k-1}{2}$ is even and $|2q+1| = \left| 2p+1 - \frac{k-1}{2} \right|$ or $|2q+1| = \left| 2p+1 + \frac{k-1}{2} \right|$, leading to

$$P_{i2} = 2\pi r_i \sin(k_{xm} X_i) \sin(k_{yn} Y_i) \cdot \sum_{p=0}^{\infty} (-1)^p J_{2p+1}(k_{xm} r_i) \left[J_{2p+1+\frac{k-1}{2}}(k_{yn} r_i) + J_{-(2p+1)+\frac{k-1}{2}}(k_{yn} r_i) \right] \quad (35)$$

P_{i3} with odd order basis function is expressed as

$$P_{i3} = -\cos(k_{xm} X_i) \sin(k_{yn} Y_i) \cdot \sum_{p=-\infty}^{\infty} \sum_{q=-\infty}^{\infty} \left\{ (-1)^p J_{2p}(k_{xm} r_i) J_{2q+1}(k_{yn} r_i) \cdot \int_0^{2\pi} \frac{1}{2} \left[\sin\left(\frac{k-1}{2} - 2p\right)\theta + \sin\left(\frac{k-1}{2} + 2p\right)\theta \right] \sin[(2q+1)\theta] r_i d\theta \right\} \quad (36)$$

The P_{i3} is only non-zero when $\frac{k-1}{2}$ is odd and $|2q+1| = \left| \frac{k-1}{2} - 2p \right|$ or $|2q+1| = \left| \frac{k-1}{2} + 2p \right|$, leading to

$$P_{i3} = -2\pi r_i \cos(k_{xm} X_i) \sin(k_{yn} Y_i) \cdot \left\{ J_0(k_{xm} r_i) J_{\frac{k-1}{2}}(k_{yn} r_i) + \sum_{p=1}^{\infty} (-1)^p J_{2p}(k_{xm} r_i) \left[J_{2p+\frac{k-1}{2}}(k_{yn} r_i) + J_{-2p+\frac{k-1}{2}}(k_{yn} r_i) \right] \right\} \quad (37)$$

When the odd order basis function is involved, P_{i1} and P_{i4} in (20) are similarly solved as

$$P_{i1} = P_{i4} = 0 \quad (38)$$

The integral for odd order basis function is obtained as

$$T_{i,odd} = P_{i1} + P_{i2} + P_{i3} + P_{i4} = \begin{cases} P_{i2}, & \frac{k-1}{2} \text{ is even} \\ P_{i3}, & \frac{k-1}{2} \text{ is odd} \end{cases} \quad (39)$$

The integral for T_j can be similarly solved. The expressions for T_j are not duplicated here due to the page limit. For convenience the modal inductance element \tilde{L}_{mn} in (11) are expressed in the Table 3.1 and the partial inductance $L_{partial,ij}$ can be analytically obtained in(19).

3.1.4. Physical Loop Inductance Extraction. There are a large element count in the partial inductance matrix. A circuit reduction approach is proposed to extract the physical loop inductance. The voltage and current for BGA ball structure are illustrated in Figure 3.3. I_1 to I_M are current flowing through signal balls. I_{M+1} to I_{M+N} are current flowing through ground balls. Voltage is similarly defined for signal balls and ground balls.

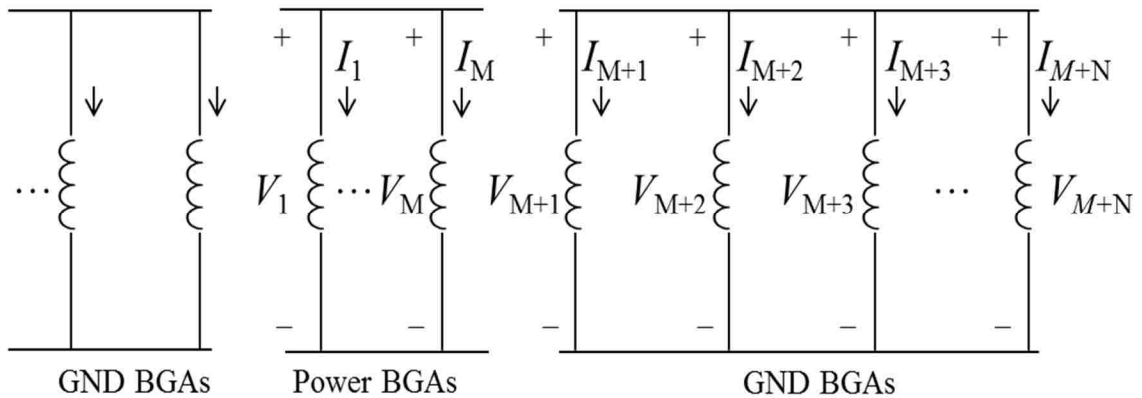


Figure 3.3. The illustration of voltage and current for BGA balls.

Table 3.1. Modal inductance element

	0 order basis function for i^{th} conductor	even order basis function for i^{th} conductor	odd order basis function for i^{th} conductor
0 order basis function for j^{th} conductor	$\sum_{m=0}^{\infty} \sum_{n=0}^{\infty} K \cdot T_{i,0} T_{j,0}$	$\sum_{m=0}^{\infty} \sum_{n=0}^{\infty} K \cdot T_{i,\text{even}} T_{j,0}$	$\sum_{m=0}^{\infty} \sum_{n=0}^{\infty} K \cdot T_{i,\text{odd}} T_{j,0}$
even order basis function for j^{th} conductor	$\sum_{m=0}^{\infty} \sum_{n=0}^{\infty} K \cdot T_{i,0} T_{j,\text{even}}$	$\sum_{m=0}^{\infty} \sum_{n=0}^{\infty} K \cdot T_{i,\text{even}} T_{j,\text{even}}$	$\sum_{m=0}^{\infty} \sum_{n=0}^{\infty} K \cdot T_{i,\text{odd}} T_{j,\text{even}}$
odd order basis function for j^{th} conductor	$\sum_{m=0}^{\infty} \sum_{n=0}^{\infty} K \cdot T_{i,0} T_{j,\text{odd}}$	$\sum_{m=0}^{\infty} \sum_{n=0}^{\infty} K \cdot T_{i,\text{even}} T_{j,\text{odd}}$	$\sum_{m=0}^{\infty} \sum_{n=0}^{\infty} K \cdot T_{i,\text{odd}} T_{j,\text{odd}}$

The KVL relationship is established as

$$\begin{bmatrix} V_1 \\ \vdots \\ V_M \\ V_{M+1} \\ \vdots \\ V_{M+N} \end{bmatrix} = j\omega [L_{\text{partial}}] \begin{bmatrix} I_1 \\ \vdots \\ I_M \\ I_{M+1} \\ \vdots \\ I_{M+N} \end{bmatrix} \quad (40)$$

where $[L_{partial}]$ is the partial inductance matrix obtained from (19). M and N are the total number of signal BGA balls and ground BGA balls, respectively.

For further simplification, (40) is converted to

$$\begin{bmatrix} I_1 \\ \vdots \\ I_M \\ I_{M+1} \\ \vdots \\ I_{M+N} \end{bmatrix} = \frac{1}{j\omega} [\Gamma_{partial}] \begin{bmatrix} V_1 \\ \vdots \\ V_M \\ V_{M+1} \\ \vdots \\ V_{M+N} \end{bmatrix} \quad (41)$$

where $[\Gamma_{partial}] = [L_{partial}]^{-1}$

In the local area the surrounding ground BGA balls are adjacent to the signal BGA balls. It is reasonable to assume that the current flowing through power balls comes back through the ground balls. The KCL relationship is established as

$$I = I_1 + \dots + I_M = -(I_{M+1} + I_{M+2} + \dots + I_{M+N}) \quad (42)$$

The potential of the surrounding BGA balls are the same as

$$V_{M+1} = V_{M+2} = \dots = V_{M+N} = V_G \quad (43)$$

$$V_1 = V_2 = \dots = V_{M+N} = V_P \quad (44)$$

By these two conditions in (42)(43), the (41) is simplified as

$$\begin{bmatrix} I \\ -I \end{bmatrix} = \frac{1}{j\omega} \begin{bmatrix} \sum_{n=1}^N \sum_{m=1}^N \Gamma_{partial\ nm} & \sum_{n=1}^N \sum_{m=M+1}^{M+N} \Gamma_{partial\ nm} \\ \sum_{n=M+1}^{M+N} \sum_{m=1}^N \Gamma_{partial\ nm} & \sum_{n=M+1}^{M+N} \sum_{m=M+1}^{M+N} \Gamma_{partial\ nm} \end{bmatrix} \begin{bmatrix} V_P \\ V_G \end{bmatrix} \quad (45)$$

The matrix in (45) is further converted to

$$\begin{bmatrix} V_P \\ V_G \end{bmatrix} = j\omega \begin{bmatrix} L'_{partial 1,1} & L'_{partial 1,2} \\ L'_{partial 2,1} & L'_{partial 2,2} \end{bmatrix} \begin{bmatrix} I \\ -I \end{bmatrix} \quad (46)$$

where

$$[L'_{partial}] = \begin{bmatrix} \sum_{n=1}^N \sum_{m=1}^N \Gamma_{partial nm} & \sum_{n=1}^N \sum_{m=M+1}^{M+N} \Gamma_{partial nm} \\ \sum_{n=M+1}^{M+N} \sum_{m=1}^N \Gamma_{partial nm} & \sum_{n=M+1}^{M+N} \sum_{m=M+1}^{M+N} \Gamma_{partial nm} \end{bmatrix}^{-1}$$

The physical loop inductance is obtained as

$$L_{loop} = \frac{V_P - V_G}{j\omega I} = L'_{partial 1,1} - L'_{partial 1,2} + L'_{partial 2,1} + L'_{partial 2,2} \quad (47)$$

3.2. EQUIVALENT INDUCTANCE VALIDATION

The two parallel plates structure with BGA balls are studied. BGA pitch size is 40mils. BGA diameter is 24mils. BGA height is 10mils. The parallel plate with one power and one ground BGA balls is shown in Figure 3.4. The x size is 500 mils and y size is 300 mils. The power ball is located at (200mils, 100mils) and the ground ball is located at (200mils, 140mils). The loop inductance is calculated by the proposed methodology and the structure is simulated from full-wave simulation tool. The loop inductance converged with more modes involved, as shown in Figure 3.5. The extracted equivalent inductance matches with the loop inductance from HFSS simulation, 112.0 pH.

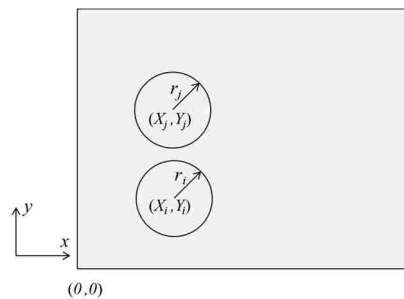


Figure 3.4. Parallel plate with one power ball and one ground ball

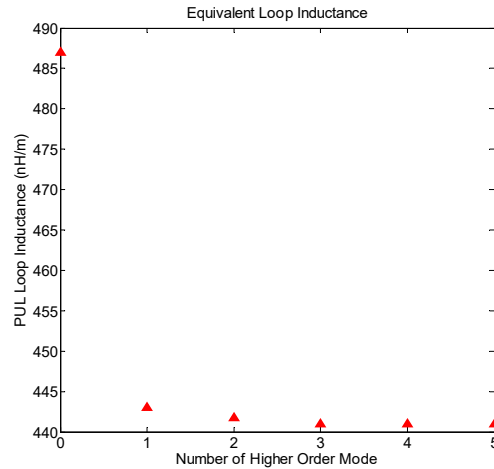


Figure 3.5. Equivalent loop inductance converges with number of modes increased

When the power/ground pairs approach toward the edge or corner of the parallel plate, the equivalent inductance increases. This is because the edge or corner of the parallel plates changes the current distribution and contribute to the equivalent inductance. The correlation between the proposed method and full-wave simulation is well maintained, as shown in Table 3.2. It shows that 1 mode is good enough for the equivalent inductance extraction.

Table 3.2. Inductance validation between proposed method and standard

Locations (mil)	(200, 100)	(40, 40)	(20,20)
Inductance from analytical calculation (0 mode)	123 pH	140.5 pH	177.2 pH
Inductance from analytical calculation (1 mode)	112.3 pH	123.0 pH	143.2 pH
Inductance from full-wave simulation	112.0 pH	123.9 pH	144.0 pH

The inductance varies at different locations on the parallel plates. The parallel plate structure with size of 400mil by 400mil is studied. BGA pitch size is 40mils. BGA diameter is 24mils. BGA height is 10mils. When the power and ground pairs are placed in column or row on the parallel plates, the equivalent inductance values are shown in Figure 3.6 and Figure 3.7, respectively. When the power and ground pairs are placed approaching to the edge or corner the equivalent inductance increases. At the middle region, the equivalent inductance is almost the same as shown in Figure 3.6 and Figure 3.7. It is because the boundary of the parallel plate has little effect for the inductance in the middle area.

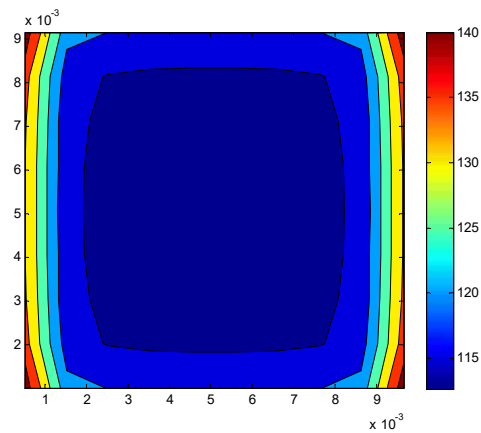


Figure 3.6. Equivalent inductance (pH) for column patterns

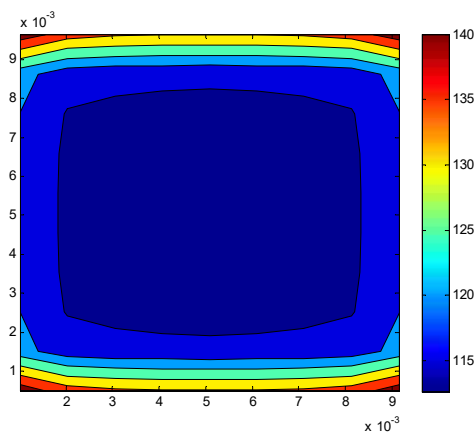


Figure 3.7. Equivalent inductance (pH) for row patterns

The proposed algorithm can be applied for selecting power and ground patterns. The parallel plate structure with size of 600mil by 500mil is studied. BGA pitch size is 40mils. BGA diameter is 24mils. BGA height is 10mils. For power and ground plates the less equivalent inductance means the less parallel plate impedance and it will results less noise on the power distributed network. The proposed method is used to select the structure of less equivalent inductance. Two different patterns are studied, as shown in Figure 3.8 and Figure 3.9. The equivalent inductance is obtained by the proposed method and full-wave simulation, as shown in Table 3.3. It is shown that the alternate power and ground pattern gives less inductance and is better for the power distributed network design.

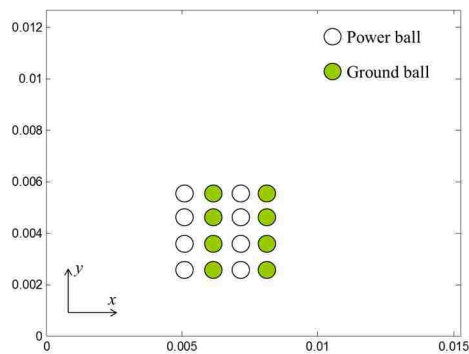


Figure 3.8. Column BGA ball patterns

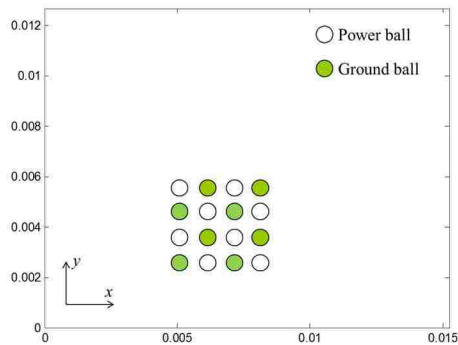


Figure 3.9. Alternate BGA ball patterns

Table 3.3 Equivalent inductance for different patterns

Pattern type	Column	Alternate
Inductance from analytical calculation	14.2 pF	8.4 pF
Inductance from full-wave simulation	14.0 pF	8.6 pF

The parallel plates with BGA balls in between is investigated. The equivalent inductance is obtained from the modal-based cavity methodology. The effect of the non-uniformly distributed current is deliberately considered in the proposed approach. The equivalent inductance is validated by full-wave simulations. When the power and ground pairs are approaching to the edge or corner of the parallel plates, the inductance will increase. The proposed method is also used to optimize the power and ground patterns in power distributed network design.

BIBLIOGRAPHY

- [1] J. Fan, X. Ye, J. Kim, B. Archambeault, and A. Orlandi, "Signal integrity design for high-speed digital circuits: progress and directions," *IEEE Trans. Electromagn. Compat.*, vol. 52, no. 2, pp 392-400, May 2010.
- [2] B. Archambeault, C. Brench, and S. Connor, "Review of printed-circuit board level EMI/EMC issues and tools," *IEEE Trans. Electromagn. Compat.*, vol. 52, no. 2, pp 455-461, May 2010.
- [3] T. Wu, F. Buesink, and F. Canavero, "Overview of signal integrity and EMC design technologies on PCB: fundamentals and latest progress," *IEEE Trans. Electromagn. Compat.*, vol. 55, no. 4, pp 624-638, Aug. 2013.
- [4] M. Swaminathan, D. Chung, S. Grivert-Talocia, K. Bharath, V. Laddha, and J. Xie, "Designing and modeling for power integrity," *IEEE Trans. Electromagn. Compat.*, vol. 52, no. 2, pp 288-310, May 2010.
- [5] E. Li, X. Wei, A. Cangellaris, E. Liu, Y. Zhang, M. D'Amore, J. Kim, and T. Sudo, "Progress Review of Electromagnetic Compatibility Analysis Technologies for Packages, Printed Circuit Boards, and Novel Interconnects," *IEEE Trans. Electromagn. Compat.*, vol. 52, no. 2, pp 248-265, May 2010.
- [6] S. Jin, J. Zhang, and J. Fan, "Optimization of the transition from connector to PCB board," in *Proc. IEEE Int. Symp. EMC*, Denver, CO, Aug. 5-9, 2013, pp. 192-196.
- [7] Y. Zhang, and J. Fan, "An Intrinsic Circuit Model for Multiple Vias in an Irregular Plate Pair Through Rigorous Electromagnetic Analysis," *IEEE Trans. Microw. Theory Tech.*, vol. 58, no. 8, Aug. 2010.
- [8] S. Jin, J. Zhang, J. Lim, K. Qiu, R. Brooks, and J. Fan, "Analytical Equivalent Circuit Modeling for Multiple Core Vias in a High-Speed Package," in *Proc. IEEE Int. Symp. EMC*, Ottawa, CN, July. 25-29, 2016, pp 233-238.
- [9] L. Ye, C. Li, X. Sun, S. Jin, B. Chen, X. Ye, and J. Fan, "Thru-Reflect-Line Calibration technique: error analysis for characteristic impedance variations in the line standards," *IEEE Trans. On Electromagnetic Compatibility*, Vol. 59, no. 3, pp 779-788, Jun. 2016.
- [10] B. Chen, M. Tsiklauri, C. Wu, S. Jin, J. Fan, X. Ye and B. Samaras, "Analytical and numerical sensitivity analyses of fixtures de-embedding," in *Proc. IEEE Int. Symp. EMC*, Ottawa, CN, July. 25-29, 2016, pp 440-444.

- [11] B. Chen, X. Ye, Q. Huang, S. Jin and J. Fan “Thru-line de-embedding (TLD), an accurate and simplified fixture removal method with self-validating line standard” in DesignCon, 2016.
- [12] M. A. Stuchly, and S. S. Stuchly, “Coaxial line reflection methods for measuring dielectric properties of biological substances at radio and microwave frequencies,” *IEEE Trans. Instrument and Measurement*, vol. 29, no. 3, pp 176-183, Sep. 1980.
- [13] D. V. Balckham, and R. D. Pollard, “An improved technique for permittivity measurement using a coaxial probe,” *IEEE Trans. Instrument and Measurement.*, vol. 46, no. 5, pp 1093-1099, Oct. 1997.
- [14] G. P. Otto, and W. C. Chew, “Improved calibration of a large open-ended coaxial probe for dielectric measurements,” *IEEE Trans. Instrument and Measurement.*, vol. 40, no. 4, pp 742-746, Oct. 1991.
- [15] M. Arai, J. G. P. Binner, T. E. Cross, “Estimating errors due to sample surface roughness in microwave complex permittivity measurements obtained using a coaxial probe,” *Electron Letters*, vol. 31, no. 2, pp 115-117, 1995.
- [16] S.-H. Chao, “An uncertainty analysis for the measurement of microwave conductivity and dielectric constant by the short-circuited line method,” *IEEE Trans. Instrum. Meas.*, vol. IM-35, pp. 36–41, Mar. 1986.
- [17] L. P. Ligthart, “A fast computational technique for accurate permittivity determination using transmission-line method,” *IEEE Trans. Microwave Theory Tech.*, vol. MTT-31, pp. 249–254, Mar. 1983.
- [18] A.-H. Boughriet, Ch. Legrand, and A. Chapoton, “Noniterative stable transmission/reflection method for low-loss material complex Permittivity determination,” *IEEE Trans. Microwave Theory Tech.*, vol. 45, pp 52–57, Jan. 1997.
- [19] J. Baker-Jarvis, M. Janezic, B. Riddle, C. L. Holloway, N. G. Paulter, and J. E. Blendell, “Dielectric and conductor-loss characterization and measurements on electronic packing materials,” Tech. Note 1520, NIST Boulder, CO, 2001.
- [20] D. K. Ghodgaonkar, V. V. Varadan, and V. K. Varadan, “A free space method for measurement of dielectric constants and loss tangents at microwave frequencies,” *IEEE Trans. Instrument and Measurement.*, vol. 38, no. 3, pp 789-793, June. 1989.
- [21] V. V. Komarov, and V. V. Yakovlev, “Modeling control over determination of dielectric properties by perturbation technique,” *Microwave Opt. Technol. Lett.* vol. 39, pp 443-446, 2003.

- [22] L. Chen, C. K. Ong, and B. T. Tan, Amendment of cavity perturbation method for permittivity measurement of extremely low-loss dielectrics, *IEEE Trans. Instrum. Meas.* vol. 48, pp 1031-1037, 1999.
- [23] J. Krupka, D Cros, M. Auburg, and P. Guillon, "Study of whispering gallery modes in anisotropic single-crystal dielectric resonators," *IEEE Trans. Microwave Theory Tech.*, vol. 42, pp 56-61, 1994.
- [24] IPC-TM-650, 2.5.5.5, March1998.
- [25] S. Jin, X. Fang, B. Chen, H. Gao, X. Ye and J. Fan, "Validating the transmission-line based material property extraction procedure including surface roughness for multilayer PCBs using simulations," in *Proc. IEEE Int. Symp. EMC*, Ottawa, CN, July. 25-29, 2016, pp 472-477.
- [26] L. Hua, B. Chen, S. Jin, M. Koledinstseva, J. Lim, K. Qiu, R. Brooks, J. Zhang, K. Shringarpure, and J. Fan, "Characterization of PCB Dielectric Properties Using Two Striplines on the Same Board," in *Proc. IEEE Int. Symp. EMC*, Raleigh, NC, Aug. 4-8, 2014, pp. 809-814.
- [27] X. Guo, Han. Gao, G. Shen, Q. Liu, V. khilkevich, J. Drewniak, S. De, S. Hinaga and D. Yanagawa, "Design Methodology for Behavioral Surface Roughness Model," in *Proc. IEEE Int. Symp. EMC*, Ottawa, ON, July 25-29, 2016, pp 927-931.
- [28] A. Koul, M. Y. Koledintseva, S. Hinaga, and J. L. Drewniak, "Differential Extrapolation Method for Separating Dielectric and Rough Conductor Losses in Printed Circuit Boards," *IEEE Trans. Electromagn. Compat.*, vol. 54, no. 2, pp 421-433, April 2012.
- [29] X. Tian, Y. Zhang, J. Lim, K. Qiu, R. Brooks, J. Zhang, and J. Fan, "Numerical investigation of glass-weave effects on high-speed interconnects in printed circuit board," in *Proc. IEEE Int. Symp. EMC*, Raleigh, NC, Aug. 4-8, 2014, pp. 475-479.
- [30] M. Y. Koledinstseva, S. K. Patil, R. W. Schwartz, W. Huebner, K. N. Rozanov, and J. Chen, "Prediction of Effective Permittivity of Diphasic Dielectrics as a Function of Frequency," *IEEE Trans. On Dielectrics and Electrical Insulation*, vol. 16, no. 3, Jun 2009.
- [31] M. Y. Koledinstseva, J. L. Drewniak, S. Hinaga, "Effect of anisotropy on extracted dielectric properties of PCB laminate dielectrics," *IEEE Electromagnetic Compatibility*, Aug 2011.

- [32] K. N. Rozanov, M. Y. Koledinstseva, “Analytical representations for frequency dependences of microwave permeability,” *IEEE Electromagnetic Compatibility*, Aug 2012.
- [33] M. Y. Koledinstseva, A. Koul, S. Hinaga, J. L. Drewniak, “Differential and extrapolation techniques for extracting dielectric loss of printed circuit board laminates,” *Microwave Symposium Digest (MTT)*, Jun 2011.
- [34] M. Y. Koledinstseva, T. Vincent, A. Ciccomancini, and S. Hinaga, “Method of effective roughness dielectric in a PCB: measurement and full-wave simulation verification,” *IEEE Trans. Electromagn. Compat.*, vol. 57, no. 4, pp 807-814, Aug 2015.
- [35] M. Y. Koledinstseva, A. V. Rakov, A. I. Koledinstseva, J. L. Drewniak, and S. Hinaga, “Improved Experiment-Based Technique to Characterize Dielectric Properties of Printed Circuit Boards,” *IEEE Trans. Electromagn. Compat.*, vol. 56, no. 6, pp 1559-1566, Dec 2014.
- [36] A. Koul, M. Y. Koledintseva, S. Hinaga, and J. L. Drewniak, “Differential Extrapolation Method for Separating Dielectric and Rough Conductor Losses in Printed Circuit Boards,” *IEEE Trans. Electromagn. Compat.*, vol. 54, no. 2, pp 421-433, April 2012.
- [37] J. Zhang, J. L. Drewniak, D. J. Pommerenke, M. Y. Koledintseva, R. E. DuBroff, W. Cheng, Z. Yang, Q. B. Chen, and A. Orlandi, “Causal RLGC(f) Models for Transmission Lines From Measured S -Parameters,” *IEEE Trans. Electromagn. Compat.*, vol. 52, no. 1, pp 189-198, Feb 2010.
- [38] M.Y. Koledintseva, A. Razmadze, A. Gafarov, S. De, S. Hinaga, and J.L. Drewniak, “PCB conductor surface roughness as a layer with effective material parameters”, *IEEE Symp. Electromag. Compat.*, Pittsburg, PA, 2012, pp. 138-142.
- [39] M. Koledintseva, J. Drewniak, S. Hinaga, F. Zhou, A. Koul, and A. Gafarov, “Experiment-based separation of conductor loss from dielectric loss in striplines”, *DesignCon 2011*, Santa Clara, CA, Jan. 31-Feb. 3, 2011, paper 5-TP5.
- [40] T. Wu, H. Chuang and T. Wang, “Overview of Power Integrity Solutions on Package and PCB Decoupling and EBG Isolation,” *IEEE Trans. Electromagn. Compat.*, vol. 52, no. 2, pp 346-356, 2010.
- [41] S. Jin, D. Liu, Y. Wang, B. Chen, and J. Fan, “Parallel Plates Impedance and the Equivalent Inductance Extraction by Modal Based Algorithm”. *IEEE Trans. On Electromagnetic Compatibility*.

- [42] S. Jin, B. Chen, X. Fang, H. Gao and J. Fan, "Improved "Root-Omega" method for transmission-line based material property extraction for multilayer PCBs", *IEEE Trans. on Electromagn. Compat.* Vol. 59, no. 4, pp1356-1367, Aug 2017.
- [43] J. Lim, K. S. Chow, J. Zhang, J. Zhang, K. Qiu and R. Brooks, "ASIC Package Design Optimization for 10 Gbps and Above Backplane SerDes Links," in *Proc. IEEE Int. Symp. EMC*, Aug. 6-10, 2012, pp. 199-204.
- [44] J. Lim, J. Zhang, W. Yao, K. Tseng, K. Qiu. R. Brooks and J. Fan, "ASIC Package to Board BGA Discontinuity Characterization in >10Gbps SerDes Links," in *Proc. IEEE Int. Symp. EMC*, Denver, CO, Aug. 5-9, 2013, pp. 569-574.
- [45] Wei Yao, Jane Lim, Ji Zhang, Kenneth Tseng, Kelvin Qiu, Rick Brooks, "Design of package BGA pin-out for >25Gb/s high speed SerDes considering PCB via crosstalk", *Electromagnetic Compatibility and Signal Integrity 2015 IEEE Symposium on*, pp. 111-116, 2015.
- [46] G. Graziosi, C. Somma, A. Morelli, C. M. Villa, P. J. Doriol, L. Marechal and S. G. Garreignot, "Ball Grid Array package for automotive application- strong link between design and 3D modeling" in *Proc. IEEE EMPC*, 2013, pp. 1-8.
- [47] R. Sun, C. Lin and R. Wu, "Designs of signal-ground bump-patterns for minimizing the simultaneous switching noise in a ball grid array," in *Proc. IEEE, EPEP*, 2008, pp. 15-18.
- [48] S. Jin, Y. Zhang, Y. Zhou, Y. Bai, X. Yu and J. Fan, "Conducted-emission modeling for a high-speed ECL clock buffer," in *Proc. IEEE Int. Symp. EMC*, Raleigh, NC, Aug. 4-8, 2014, pp 594-599.
- [49] S. Jin, "Constructing conducted emission models for integrated circuits", dissertation, Dept. Elect. Eng., Missouri University of Science and Technology, Rolla, MO, 2013.
- [50] Y. Wang, S. Bai, X. Guo, S. Jin, Y. Zhang, J. Eriksson, L. Qu, J. Huang and J. Fan, "Conducted-emission modeling for a switched-mode power supply (SMPS)," in *Proc. IEEE Int. Symp. EMC*, Santa Clara, CA, Mar. 15-21, 2015, pp 314-319.
- [51] T. Wang, S. Chen, C. Tsai, S. Wu, J. L. Drewniak, and T. Wu "Modeling Noise Coupling Between Package and PCB Power/Ground Planes With an Efficient 2-D FDTD/Lumped Element Method" *IEEE Trans. On Advanced Packaging*, vol. 30, no. 4, pp 864-871, Nov. 2007.
- [52] H. H. M. Ghouz and E. B. EI-Sharawy, "An Accurate Equivalent Circuit Model of flip chip and via interconnects," *IEEE Trans. On Microwave Theory and Techniques*, vol. 44, no. 12, Dec 1996.

- [53] A. E. Ruehli, "Inductance Calculations in a Complex Integrated Circuit Environment," *IBM Journal of research and development*, vol. 16, 1972.
- [54] Y. S. Cao, T. Makharashvili, J. Cho, S. Bai, S. Connor, B. Archambeault, L. J. Jiang, A. E. Ruehli, J. Fan and J. L. Drewniak, "Inductance Extraction for PCB Pre-layout Power Integrity Using PMSR Method," *IEEE Trans. Electromag. Compat.*, vol. 59, no. 4, pp. 1339-1346, Aug. 2017.
- [55] Y. S. Cao, T. Makharashvili, S. Connor, B. Archambeault, L. J. Jiang, A. E. Ruehli, J. Fan and J. L. Drewniak, "Top-layer interconnect inductance extraction for the pre-layout power integrity using the physics based model size reduction (PMSR) method," *IEEE Int. Symposium on Electromagnetic Compatibility*, Ottawa, Canada, Jul. 2016.
- [56] B. Yassini, S. Safavi-Naeini and T. Manku, "A wideband model for high density ball-grid array packages for very high speed digital circuits" in *IEEE, Symp. On ANTEM*, 2000, pp. 121-124.
- [57] I. Ndip, W. John and H. Reichl, "Effects of Discontinuities and Technological Fluctuations on the RF Performance of BGA Packages," in *IEEE proceedings electronic components and technology*, 2005, pp. 1769-1775.
- [58] I. Ndip, W. John, H. Reichl, "Efficient RF-Microwave Modeling of Discontinuities in chip packages and boards," in *IEEE European Microwave conference*, 2005.
- [59] D. Staiculescu, H. Liang, J. Laskar, J. Mather, "Full Wave Analysis and Development of Circuit Models for flip chip interconnects," in *IEEE, EPEP*, 1998, pp. 241-244.
- [60] N. Pham, B. Mutnury, E. Matoglu, M. Cases, D. N. De Araujo, "Package Model for Efficient Simulation, Design, and Characterization of High Performance electronic systems," in *IEEE, workshop on signal propagation on interconnects*, 2006, pp. 39-42.
- [61] IEEE Standard P1597, Standard for Validation of Computational Electromagnetics Computer Modeling and Simulation – Part 1, 2 2008.
- [62] A.P. Duffy, A.J.M. Martin, A Orlandi, G Antonini, T.M. Benson, M.S. Woolfson, "Feature Selective Validation (FSV) for validation of computational electromagnetics (CEM). Part I – The FSV method", *IEEE Trans. on Electromagn. Compatibility*, Vol 48, No 3, Aug 2006, pp 449 – 459.

- [63] A Orlandi, A.P. Duffy, B Archambeault, G Antonini, D.E. Coleby, S Connor “Feature Selective Validation (FSV) for validation of computational electromagnetics (CEM). Part II – Assessment of FSV performance”, *IEEE Trans. on Electromagn. Compatibility*, Vol. 48, No 3, Aug 2006, pp 460 – 467.
- [64] B. Chen, M. Qi, S. Yong, Y. Wang, J. Wang, S. Jin, Y. Bai, Y. Zhou and J. Fan “Differential integrated crosstalk noise (ICN) reduction among multiple differential BGA and via pairs by using design of experiments (DoE) method” in *Proc. IEEE Int. Symp. EMC*, Washington, DC, 2017.
- [65] Y. Wang, S. Penugonda, S. Jin and J. Fan “Variability Analysis of Crosstalk Among Differential Vias Using Polynomial-Chaos and Response Surface Methods”, *IEEE Trans. On Electromagnetic Compatibility*, Vol. 59, no. 4, pp 1368-1378, Aug 2017.
- [66] Y. Wang, S. Penugonda, S. Jin, J. Chen and J. Fan, “Variability analysis of crosstalk among pairs of differential vias using polynomial-chaos and design of experiments methods,” in *Proc. IEEE Int. Symp. EMC*, Ottawa, CN, July. 25-29, 2016, pp 222-227.
- [67] C. Mattei, A. P. Agrawal, “Electrical characterization of BGA packages,” in *electronic components and technology conference*, 1997, pp. 1098-1093.
- [68] T. Horng, S. Wu, A. Tseng, H. Huang, “electrical modeling of enhanced ball grid array packages using coupled transmission lines,” in *Electronics Letters*, 1999, pp. 1567-1569.
- [69] T. Chang, P. H. Cheng, H. C. Huang, R. S. Lee and R. Lo, “Parasitic Characteristics of BGA Packages,” in *IEEE Symp. On IC/Package Design Integration*, 1998, pp. 124-129.
- [70] D. Staiculescu, A. Pham, J. Laskar, S. Consolazio, S. Moghe, “Analysis and Performance of BGA Interconnects for RF package,” in *IEEE RFIC Symp.*, 1998, pp. 131-134.
- [71] T. S. Horng, A. Tseng, H. H. Huang, S. M. Wu, J. J. Lee, “Comparison of Advanced Measurement and Modeling Techniques for electrical characterization of ball grid array packages” in *Electronic Components and Technology Conference*, 1998, pp. 1464-1471.
- [72] D. Liu, S. Pan, B. Achkir, and J. Fan, “Fast admittance computation for TSV arrays View Document” in *Proc. IEEE Int. Symp. EMC*, Aug. 06-10, 2012.

- [73] J. S. Pak, J. Lee, H. Kim, and J. Kim, "Prediction and verification of power/ground plane edge radiation excited by through-hole signal via based on balanced TLM and via coupling model," in *Proc. Elect. Perform Electron. Packag.*, 2003, pp. 181–184.
- [74] I. Novak, "Reducing simultaneous switching noise and EMI on ground/power planes by dissipative edge termination," *IEEE Trans. Adv. Packag.*, vol. 22, no. 3, pp. 274–283, Aug. 1999.
- [75] X. D. Cai, G. I. Costache, R. Laroussi, and R. Crawhall, "Numerical extraction of partial inductance of package reference (power/ground) planes," in *Proc. IEEE Int. Symp. Electromagn. Compat.*, 1995, pp. 12–15.
- [76] K. Shringarpure, S. Pan, J. Kim, J. Fan, B. Achkir, B. Archambeault, and J. L. Drewniak, "Formulation and Network Model Reduction for Analysis of the Power Distribution Network in a Production-Level Multilayered Printed Circuit Board" *IEEE Trans. Electromagn. Compat.*, vol. 58, no. 3, pp 849-858, April 2016.
- [77] X. Duan, R. Rimolo-Donadio, H. Bruns, and C. Schuster, "Circular Ports in Parallel-Plate Waveguide Analysis With Isotropic Excitations" *IEEE Trans. Electromagn. Compat.*, vol. 54, no. 3, pp 603-612, June 2012.
- [78] J. Kim, L. Ren, and J. Fan, "Physics-based inductance extraction for via arrays in parallel planes for power distribution network design," *IEEE Trans. Microw. Theory Techn.*, vol. 58, no. 9, pp. 2434–2447, Sep. 2010.
- [79] J. Kim, K. Shringarpure, J. Fan, J. Kim, and J. L. Drewniak, "Equivalent circuit model for power bus design in multi-layer PCBs with via arrays," *IEEE Microw. Wireless Compon. Lett.*, vol. 21, no. 2, pp. 62–64, Feb 2011.
- [80] L. Ren, J. Kim, G. Feng, B. Archambeault, J. L. Knighten, J. Drewniak, and J. Fan, "Frequency-dependent via inductances for accurate power distribution network modeling," in *Proc. IEEE Int. Symp. Electromagn. Compat.*, 2009, pp. 63–68.
- [81] J. Kim, J. Fan, A. E. Ruehli, J. Kim, and J. L. Drewniak, "Inductance calculations for plane-pair area fills with vias in a power distribution network using a cavity model and partial inductances," *IEEE Trans. Microw Theory Techn.*, vol. 59, no. 8, pp. 1909–1924, Aug. 2011.
- [82] J. Xu, Y. Wang, Y. Zhang, C. Sui, B. Sen, S. Jin and J. Fan, "A Survey on Modeling Strategies for High-speed Differential Via between Two Parallel Plates", in *Proc. IEEE Int. Symp. EMC*, Washington, DC, 2017.

- [83] Y. Zhang, Y. Wang, J. Xu, C. Sui, B. Sen, S. Jin and J. Fan, “Estimating the via-plane capacitance for differential vias with shared-antipad based on analytical equations””, in *Proc. IEEE Int. Symp. EMC*, Washington, DC, 2017.
- [84] S. Jin, D. Liu, B. Chen, K. Qiu, J. Lin, R. Brooks, and J. Fan, “Analytical equivalent circuit modeling for BGA ball array in high-speed package”, *IEEE Trans. On Electromagnetic Compatibility*, Vol. 60, no. 1, pp 68-76, Feb 2018.
- [85] F. W. J. Oliver, D. W. Lozier, R. F. Boisvert, C. W. Clark, *NIST Handbook of Mathematical Functions*, Chapter 10, page 226.

VITA

Shuai Jin was born in Baishan City, Jilin Province, P.R. China. In May 2011, he received his Bachelor of Science, Biomedical Engineering in Huazhong University of Science and Technology, Wuhan, P.R. China.

In August 2011, he enrolled at the Missouri University of Science and Technology to pursue his Master's Degree in Electrical Engineering. He was a graduate research assistant in Electromagnetic Compatibility Laboratory. After finishing his Master's Degree in December 2013, he continued Ph.D degree in Electromagnetic Compatibility Laboratory. His research interests included signal integrity in high speed digital systems, power distributed network modeling, RF interference and high-speed package modeling. In December 2017, he received his Ph.D degree in Electrical Engineering from Missouri University of Science and Technology.